5-2016

Potential and timescales for oxygen depletion in coastal upwelling systems: A box-model analysis

Cheryl S. Harrison
The University of Texas Rio Grande Valley

B. Hales

S. Siedlecki

R. M. Samelson

Recommended Citation

Harrison, C. S., Hales, B., Siedlecki, S., and Samelson, R. M. (2016), Potential and timescales for oxygen depletion in coastal upwelling systems: A box-model analysis, J. Geophys. Res. Oceans, 121, 3202– 3227, doi:10.1002/2015JC011328.

AGU PUBLICATIONS

JGR

Journal of Geophysical Research: Oceans

RESEARCH ARTICLE

10.1002/2015JC011328

Key Points:
- Hypoxia is favored for large sinking rate, and largely independent of production rate
- Oxygen depletion can only be reached in meaningfully short times when productivity is rapid
- The timescale for approach to hypoxia lengthens with stronger upwelling

Correspondence to:
R. M. Samelson,
rsamelson@coas.oregonstate.edu

Citation:
Harrison, C. S., B. Hales, S. Siedlecki, and R. M. Samelson (2016), Potential and timescales for oxygen depletion in coastal upwelling systems: A box-model analysis, *J. Geophys. Res. Oceans*, *121*, 3202–3227, doi:10.1002/2015JC011328.

Received 2 OCT 2015
Accepted 20 MAR 2016
Accepted article online 23 MAR 2016
Published online 18 MAY 2016

Potential and timescales for oxygen depletion in coastal upwelling systems: A box-model analysis

C. S. Harrison[1,2], B. Hales[1], S. Siedlecki[3], and R. M. Samelson[1]

[1]CEOAS, Oregon State University, Corvallis, Oregon, USA, [2]Now at National Center for Atmospheric Research, Boulder, Colorado, USA, [3]JISAO, University of Washington, Seattle, Washington, USA

Abstract A simple box model is used to examine oxygen depletion in an idealized ocean-margin upwelling system. Near-bottom oxygen depletion is controlled by a competition between flushing with oxygenated offshore source waters and respiration of particulate organic matter produced near the surface and retained near the bottom. Upwelling-supplied nutrients are consumed in the surface box, and some surface particles sink to the bottom where they respire, consuming oxygen. Steady states characterize the potential for hypoxic near-bottom oxygen depletion; this potential is greatest for faster sinking rates, and largely independent of production timescales except in that faster production allows faster sinking. Timescales for oxygen depletion depend on upwelling and productivity differently, however, as oxygen depletion can only be reached in meaningfully short times when productivity is rapid. Hypoxia thus requires fast production, to capture upwelled nutrients, and fast sinking, to deliver the respiration potential to model bottom waters. Combining timescales allows generalizations about tendencies toward hypoxia. If timescales of sinking are comparable to or smaller than the sum of those for respiration and flushing, the steady state will generally be hypoxic, and results indicate optimal timescales and conditions exist to generate hypoxia. For example, the timescale for approach to hypoxia lengthens with stronger upwelling, since surface particle and nutrient are shunted off-shelf, in turn reducing subsurface respiration and oxygen depletion. This suggests that if upwelling winds intensify with climate change the increased forcing could offer mitigation of coastal hypoxia, even as the oxygen levels in upwelled source waters decline.

1. Introduction

Oxygen depletion leading to hypoxia and anoxia in coastal waters can negatively affect fisheries and local ecosystem functioning, particularly in benthic environments that support commercially important populations of groundfish and crustaceans [*Bailey et al*., 1985; *Chan et al*., 2008; *Keller et al*., 2015]. Bottom waters over the shelf can become hypoxic, with variability over a variety of temporal and spatial scales [*Bailey et al*., 1985; *Bailey*, 1991; *Grantham et al*., 2004; *Chan et al*., 2008; *Peterson et al*., 2013; *Adams*, 2014; *Siedlecki et al*., 2015]. In extreme cases low oxygen events lead to large areas of mortality popularly referred to as "dead zones." Such events have been reported with increasing frequency [*Grantham et al*., 2004; *Chan et al*., 2008] and associated with detrimental effects [*Keller et al*., 2015] in the Pacific Northwest, stimulating interest into processes controlling hypoxia [*Hales et al*., 2006; *Connolly et al*., 2010; *Bianucci et al*., 2011; *Adams*, 2014; *Peterson et al*., 2013; *Siedlecki et al*., 2015]. These studies indicate that both local respiration of organic matter and variations in the oxygen content of upwelled waters play a role in the seasonal development of hypoxia on shelves in the Pacific Northwest, while farther to the south along the California coast, the transport of low oxygen water masses onto the shelf and stratification are thought to be potentially more important drivers [*Bograd et al*., 2008; *Send and Nam*, 2012]. Controls over interannual variability in the severity of hypoxic events, and specifically how hypoxia in upwelling systems is related to regional and basin scale processes, still remain unclear [*Hales et al*., 2006; *McClatchie et al*., 2010; *Deutsch et al*., 2011; *Nam et al*., 2011].

In coastal upwelling systems, equatorward winds drive surface offshore Ekman flow, drawing nutrient-rich water from the ocean interior to the surface and supporting productive coastal ecosystems [*Ryther*, 1969; *Chavez and Toggweiler*, 1995; *Carr and Kearns*, 2003]. The close proximity of the seafloor to the productive coastal surface waters allows retention of oxygen-depletion potential in the coastal system, with the

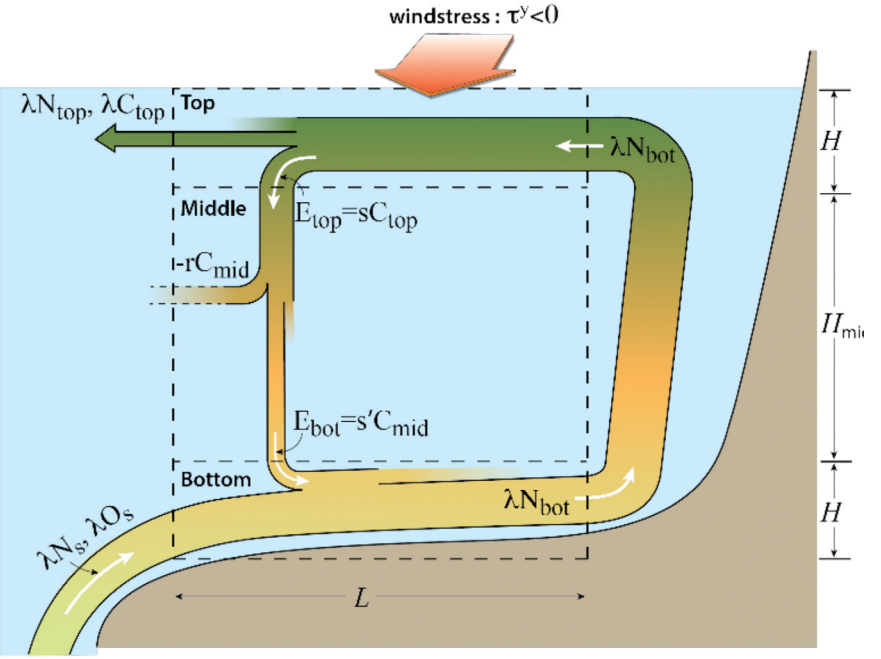

Figure 1. Schematic of box model and total nutrient cycling. Upwelling favorable wind stress drives offshore surface transport, parameterized by the inverse shelf-transit or volume-renewal time λ, which is a function of the wind stress τ^y, the shelf width L, and the depth of the surface (and bottom) layer H. Upwelling brings nutrients to the surface, driving particle production. Some of the upwelled nutrient flux is lost offshore as nutrients (λN_{top}) or particles (λC_{top}), some exported to the bottom as sinking particle flux (E_{bot}), and some remineralized in the midwatercolumn (rC_{mid}). Offshore surface transport is compensated by onshore transport in the bottom box, bringing source nutrients (N_s) and oxygen (O_s) into the system.

retention fraction determined by conversion of upwelled nutrient to sinking organic matter that is subsequently respired within shelf waters rather than transported offshore. The source waters for this upwelling originate from the low-oxygen ocean interior and so are subject to the mechanisms for interior oxygen depletion described above. Regional variations in wind forcing and other conditions also contribute to the variability of oxygen levels within these systems. For example, in the California Current System, the shelves are wider, upwelling weaker, and freshwater sources more prevalent in the north than in the south, all of which can affect local levels of hypoxia.

In general, the extent and rate of development of hypoxia in coastal upwelling systems depends on the timescales of competing physical and biogeochemical processes that determine the flushing of these waters and the retention within them of organic matter that represents an effective potential source of respiratory oxygen consumption. The role of source water oxygen level is relatively direct and has been highlighted as a potential driver of hypoxia in upwelling regions [*Grantham et al*., 2004; *Bograd et al*., 2008; *McClatchie et al*., 2010; *Peterson et al*., 2013]. The factors that determine the rate and extent of on-shelf oxygen depletion are less understood, although the interplay between respiration and flushing is clearly important [*Adams et al*., 2013; *Siedlecki et al*., 2015].

Coupled numerical models have begun to give useful insights into the local dynamics of hypoxia in specific regions and systems [e.g., *Peña et al*., 2010; *Siedlecki et al*., 2015], but we take a different approach here. We use instead a highly simplified box-type model to explore systematically the potential for oxygen depletion in a broad class of upwelling systems, and to suggest general relationships between the timescales of physical flushing and the biogeochemical processes of production, respiration, and sinking that determine this potential. Our goal is not to provide a specific prediction for hypoxic behavior in a particular region at a particular time, but instead to develop a broad quantitative characterization of the relative roles of the fundamental rates and parameters in controlling the susceptibility of upwelling systems to hypoxia. We hope thereby also to enable a general assessment of the likelihood of hypoxic behavior in any given system for which a representative set of rates and parameters can be constructed or estimated.

With this goal in mind, we construct a highly simplified box model of the upwelling system, and then subject it to a thorough analysis in model-parameter space, the broadest summary aspects of which necessarily involve a relatively abstract framework. The main results are given in sections 3–5. Section 3 presents the most concrete and accessible description, in terms of two specific examples. Section 4 progresses to a discussion of two abstracted elements, steady-state depletion and an exponential timescale for evolution toward hypoxia, and their dependence on process rates and parameters. Section 5 collects the most general results, framed in terms of relative – rather than absolute – process rates, and broadly describing the susceptibility of the model system to hypoxia through derived criteria on these relative rates.

2. Model Description

2.1. Overview

The model represents integral balances for a cross-shelf slice of an alongshore-uniform continental shelf domain under upwelling conditions (Figure 1). Motivated by observations in upwelling systems of elevated particulate organic carbon over the shelf in both the surface and bottom boundary layers [e.g., *Karp-Boss et al*., 2004; *Hales et al*., 2006; *Holser et al*., 2011] separated by a midwater layer with low particle abundance, we partition the midshelf by depth into three control volumes, or boxes. The top box, with thickness H, represents a surface boundary layer, where both offshore physical transport and particulate organic matter production are confined. The bottom box, taken to have the same thickness H, represents the bottom boundary layer, in which onshore upwelling transport is confined. The interior water column between the surface and bottom boundary layers forms a middle box, with thickness H_{mid}, so that the ratio between the middle and boundary layer boxes is $\delta_H = H/H_{mid}$. A single nominal cross-shelf width L is specified for all three boxes, and all modeled balances and quantities are computed per unit alongshore distance.

The model state variables are: $\Delta O_{bot} = O_s - O_{bot}$, the depletion of bottom-box oxygen concentration O_{bot} from its fixed offshore value O_s; C_{bot} and N_{bot}, the bottom-box particle and generic nutrient concentrations, respectively; and C_{top} and N_{top}, the corresponding top-box concentrations. The model equations are

$$\frac{d\Delta O_{bot}}{dt} = \frac{v}{\gamma} r C_{bot} - \lambda \Delta O_{bot}, \tag{2.1}$$

$$\frac{dC_{bot}}{dt} = E_{bot} - r C_{bot}, \tag{2.2}$$

$$\frac{dN_{bot}}{dt} = \frac{r}{\gamma} C_{bot} + \lambda (N_s - N_{bot}), \tag{2.3}$$

$$\frac{dC_{top}}{dt} = \left(p \frac{N_{top}}{K + N_{top}} - r - s - \lambda \right) C_{top}, \quad \text{and} \tag{2.4}$$

$$\frac{dN_{top}}{dt} = \frac{1}{\gamma} \left(r - p \frac{N_{top}}{K + N_{top}} \right) C_{top} + \lambda (N_{bot} - N_{top}), \tag{2.5}$$

where the sinking flux into the bottom box, E_{bot} in (2.2), is given in terms of C_{top} by

$$E_{bot}(t) = \delta s^2 \int_0^t e^{-(r+\delta s)(t-t')} C_{top}(t') dt' \ . \tag{2.6}$$

The middle box is linked to the top and bottom boxes by particle sinking fluxes but is taken otherwise to be isolated, and the middle-box particle balance can thus be entirely represented by the integral transform (2.6) (see Appendix A, equation (A1)). The derivation of (2.1)-(2.6) and the definitions of the parameters in these equations are summarized in section 2.2. Parameter values are discussed in section 2.3.

2.2. Formulation and Parameter Definition

The physical circulation comprises wind-driven cross-shore Ekman transport U_E [e.g., *Gill*, 1982] per unit alongshore distance, analogous to an upwelling index [*Schwing et al*., 1996]. Here $U_E < 0$ corresponds to equatorward wind forcing and upwelling conditions, with offshore transport out of the top box and compensating onshore transport into the bottom box and upwelling from the bottom box to the top box. In all

cases $U_E \leq 0$, so that downwelling never occurs. Normalizing the transport by cross-shelf box area LH yields an upwelling rate λ (d^{-1}):

$$\lambda = -U_E/LH \tag{2.7}$$

Since all offshore transport from the top box is compensated by onshore flow to the bottom box, and top and bottom boxes are prescribed to have the same volume, λ is also the flushing rate of the bottom box. For simplicity, downwelling and mixing between the boxes are not considered, consistent with the focus on advectively driven upwelling systems.

The dissolved O_2 concentration in the bottom box is denoted O_{bot} (mmol m^{-3}), and its rate of change is determined by the respiration of bottom-box particles, with particle concentration C_{bot} (mmol m^{-3}), and the divergence of onshore and upward upwelling-driven advective oxygen fluxes:

$$\frac{dO_{bot}}{dt} = \lambda(O_s - O_{bot}) - \frac{v}{\gamma} r C_{bot}. \tag{2.8}$$

In (2.8), the constants r (d^{-1}) and O_s (mmol m^{-3}) are, respectively, the carbon-specific particle respiration rate and the oxygen concentration of the deep offshore source waters drawn into the bottom box by the upwelling circulation. The ratio v/γ represents the stoichiometric proportion of O_2 consumed per unit organic carbon during respiration, represented in terms of the ratios v, of O_2 consumed to nitrogen released during respiration, and γ, of organic carbon to nitrogen in average marine organic matter, with nominal, fixed values $v=10$ and $\gamma=7$, so that $v/\gamma = 10/7 \approx 1.4$ in (2.8). Equation (2.8) can be rewritten in terms of the oxygen depletion from the constant offshore value, $\Delta O_{bot} = O_s - O_{bot}$, yielding (2.1). This relative depletion is independent of O_s, and emphasizes on-shelf processes. Since downwelling and mixing between the boxes are not allowed, oxygen enters the bottom box only from offshore and the oxygen mass balances for the other boxes can be ignored.

Determination of C_{bot} (mmol m^{-3}) is necessary for solution of (2.8) or (2.1), and this in turn requires linkage to the particle production in the surface box and its export to the bottom box by sinking. The balance (2.2) between respiration and the incoming sinking flux E_{bot} (mmol m^{-3} d^{-1}) controls the bottom-box particle concentration. Essentially all particles incorporated in surficial sediments are respired on short timescales very near the sediment-water interface, with respiration products rapidly returned to overlying waters [see *Siedlecki et al.*, 2015; *Bianucci et al.*, 2011], so no explicit term is included representing loss of C_{bot} through long-term sediment burial, and sediment respiration is assumed to be incorporated in the bottom-box respiration term.

In the top box, nutrients are taken up and transformed directly into particles, and intermediate biological processes are only implicitly represented. As described by (2.4), C_{top} production thus proceeds via a particle-specific rate constant, p (d^{-1}), scaled by a Monod-form dependence on the concentration of a generic nutrient N_{top} (mmol m^{-3}), with half-saturation constant K (mmol m^{-3}). C_{top} is lost in proportion to its concentration by respiration at the rate r, by export through vertical sinking at the specific rate s (d^{-1}), and by transport offshore at the upwelling rate λ (d^{-1}). Particles are assumed to sink faster than the upwelling velocity, so that there is no upwelling flux of particles. The specific sinking rate $s = S/H$, where S (m d^{-1}) is the sinking speed.

The two boxes are linked by the dependence of the incoming particle flux E_{bot} (2.6) on the sinking export flux sC_{top}. These fluxes would be instantaneously equal if the middle box were absent; however, the sinking flux is attenuated by respiration and temporally delayed during transit through the middle box. In (2.6), δ is the ratio of middle-box and top-box specific sinking rates,

$$\delta = s'/s, \tag{2.9}$$

where $s' = S'/H_{\mathrm{mid}}$ and S' is the middle-box sinking speed, so that $\delta = \delta_H$ when $S' = S$. The incoming sinking flux E_{bot} will differ most from the surface sinking flux for rapid respiration (large r) and long settling transit time (small δs), which give large attenuation and delay (Appendix A).

While surface nutrient levels are often high under upwelling conditions, they can fall to levels near K that limit production, and must be modeled explicitly. The top-box (N_{top}) and bottom-box (N_{bot}) nutrient balances, (2.5) and (2.3), include the same particle growth and respiration terms seen in (2.4) and (2.2), with

Table 1. Fixed Model Parameters

Parameter	Value	Description
N_s	35 mmol m^{-3}	Upwelled source-water nutrient concentration
$C_{top,0}$	1 mmol m^{-3}	Top-box initial particle concentration
$N_{top,0}$	5 mmol m^{-3}	Top-box initial nutrient concentration
$N_{bot,0}$	35 mmol m^{-3}	Bottom-box initial nutrient concentration
$O_{bot,0}$	100 mmol m^{-3}	Bottom-box initial O_2 concentration
ΔO_{hyp}	40 mmol m^{-3}	O_2 depletion indicating hypoxia
ΔO_{an}	100 mmol m^{-3}	O_2 depletion indicating extreme hypoxia

opposite sign and scaled by γ. Nutrient is supplied to the top box by upwelling from the bottom box and transported offshore with the flushing rate λ; it is supplied to the bottom box from offshore source waters with concentration N_s and upwelled with the same timescale.

2.3. Parameter Values

The model as formulated depends only on the rate constants λ, p, s, and r, the dimensionless specific-sinking-rate ratio δ, the half-saturation constant K, and the initial (to be denoted by subscript 0, e.g., C_{top0}) and source-water (subscript s, e.g., O_s) values of the modeled concentrations. The initial and source-water concentrations were fixed at nominal values (Table 1), based on previous observations of Oregon coast source and on-shelf water nitrate [*Hales et al*., 2005] oxygen [*Hales et al*., 2006] and particulate organic carbon [*Karp-Boss et al*., 2004; *Hales et al*., 2006; *Holser et al*., 2011]. The dependence on K was examined for a wide range of values, $0 < K < 2$ mmol m^{-3}. In addition, two specific levels of bottom oxygen depletion were used as indicators for hypoxia, 40 and 100 mmol m^{-3}, which for a nominal source-water oxygen concentration of 100 mmol m^{-3} correspond respectively to moderate hypoxia (60 mmol m^{-3} O_2) and severe hypoxia or anoxia (0 mmol m^{-3} O_2). Model geometry was fixed, with $H = 20$ m and total depth 100 m, so that $\delta = 1/3$ when $S' = S$ (Table 2), but the general dependence on δ was also examined. The rate constants must be positive and are further constrained by observational or laboratory estimates. The respiration rate r was fixed at 0.2 d^{-1}, consistent with observations of particle-specific respiration rates for the Oregon coastal upwelling system [*Wetz et al*., 2008; B. Hales, unpublished manuscript; F. Chan, personal communication].

Other parameters were allowed to vary to reflect ranges of possible upwelling and biogeochemical rates. We considered upwelling rates λ from 0.02 to 0.4 d^{-1}, spanning a range of conditions from weak upwelling over a broad shelf (such as the Galician upwelling system [e.g., *Herrera et al*., 2008]) to strong upwelling over a narrow shelf (such as the central-northern California system [e.g., *Chavez and Messié*, 2009]). For example, upwelling wind stress 0.1 N m^{-3} and box-width $L = 20$ km gives $U_E \approx 0.5$ m^2 s^{-1} and $\lambda \approx 0.1$ d^{-1}. In all cases, excepting a brief discussion of preliminary results for variable forcing, the upwelling rate λ was taken to be constant in time. We considered ranges of p from near 0 up to 2 d^{-1}, capturing the fastest reported doubling times for fast-growing diatoms [*Barber and Chavez*, 1991; *Lindley et al*., 1995; *Dugdale and Wilkerson*, 1998; *Chai et al*., 2002]. We considered sinking rates s ranging from near 0 up to 1 d^{-1}, which, for the fixed 20-m thickness of the surface box, corresponds to a maximum physical sinking velocity of 20 m d^{-1}, consistent with observed sinking velocities for large individual diatoms [*Jamart et al*., 1977; *McDonnell and Buesseler*, 2010, 2012; *Iversen and Ploug*, 2010, 2013]. Part of the analysis is based on relative rates, further generalizing these nominal parameter ranges.

To contrast the magnitudes and timescales of bottom oxygen depletion for systems dominated by rapidly growing and sinking particles and by slowly growing and sinking particles, two specific sets of biogeochemical rates were chosen as example cases (Table 2), denoted FP ('Fast Particles') and SP ('Slow Particles'). The FP case represents a system dominated by rapidly growing and sinking plankton with a higher nutrient half-saturation constant, such as coastal diatoms, which are observed to dominate the biomass of the initial production response to coastal upwelling [e.g., *Dugdale and Wilkerson*, 1998]. The SP case represents a system with a slower biological response to upwelled nutrients and much slower particle sinking velocities, but a smaller half-saturation constant and thus less sensitivity to nutrient level.

Table 2. Variable Model Parameters With Nominal or Case-Specific Values

Parameter	Nominal or Case-Specific Value	Description
δ	1/3	Ratio of specific sinking rates
r	0.2 d^{-1}	Respiration rate
λ	0.1 d^{-1}	Upwelling rate
p ("Fast Particle")	1.1 d^{-1}	specific particle growth rate
p ("Slow Particle")	0.45 d^{-1}	specific particle growth rate
s ("Fast Particle")	0.5 d^{-1}	specific sinking rate.
s ("Slow Particle")	0.05 d^{-1}	specific sinking rate.
K ("Fast Particle")	1 mmol m^{-3}	limiting nutrient level
K ("Slow Particle")	0.25 mmol m^{-3}	limiting nutrient level

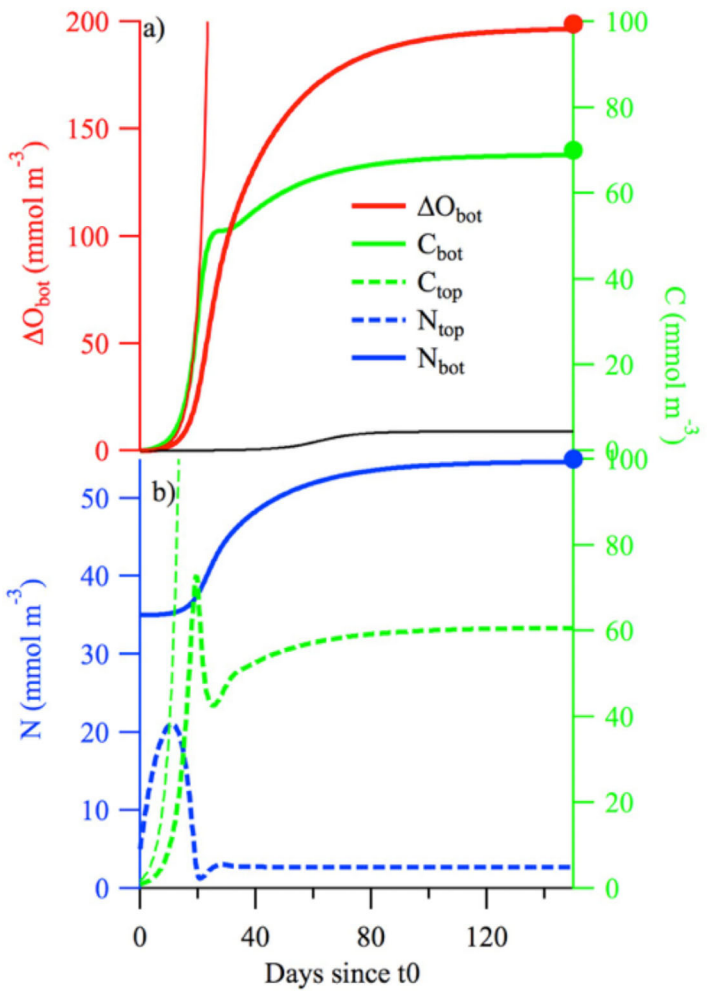

Figure 2. Temporal evolution of model with constant forcing at $\lambda = 0.1\ d^{-1}$ with other parameters fixed at the FP parameter-set values. (a) Evolution of the deep-box oxygen depletion and particle accumulation; and (b) evolution of the surface particle accumulation and surface and deep nutrient concentrations. Other curves are shown for comparison: the deep-box oxygen depletion predicted from the exponential approximation (light red line, Figure 2a); the oxygen depletion for the SP parameter set (light black line, same as heavy red line in Figure 3a); and the C_{top} predicted from the exponential approximation (Figure 2b, light dashed green line). Large solid circles at day 150 represent the ΔO_{bot}, C_{bot}, and N_{bot} steady state solutions.

3. Results: FP and SP Examples

3.1. Temporal Evolution

In this section, the temporal evolution of the selected-parameter FP and SP cases (section 2.3, Table 2) is considered for a simple seasonal upwelling scenario, in which the system is initialized with low surface particle and nutrient concentrations and then forced with constant upwelling-favorable winds, $\lambda = 0.1\ d^{-1}$ for 150 days, a period comparable to the maximal extent of a midlatitude eastern boundary upwelling season. These examples illustrate the response of the bottom-box oxygen depletion (ΔO_{bot}; equation (2.1)) to the bottom-box particle dynamics, and the relation of these to the evolution of the surface particle dynamics, and, in turn, the coupling of both to the upwelling circulation.

After 10 days of sustained upwelling, ΔO_{bot} even in the FP case has reached only ~2 mmol m^{-3} (Figure 2a), but, after 20 days, it reaches nearly 30 mmol m^{-3}. The moderate hypoxia threshold ($\Delta O_{bot} = 40$ mmol m^{-3}), is surpassed by day 22, and the extreme hypoxia threshold ($\Delta O_{bot} = 100$ mmol m^{-3}) by day 31. The final ΔO_{bot} for this scenario is over 200 mmol m^{-3}, more than enough to deplete all of the oxygen from a broad spectrum of ocean interior waters. This rapid and intense depletion suggests that the near-bottom waters of a simple upwelling system dominated by fast growing and sinking particles and subject to a constant upwelling forcing would spend the majority of the upwelling season in an anoxic state.

Oxygen depletion is driven by the respiration of accumulating organic particles in the bottom layer (C_{bot}). To understand the mechanism behind this behavior, it is useful to examine more closely the evolution of the particle concentrations. The rapid rise in ΔO_{bot} for FP is a delayed response to the rise in C_{bot}, which builds from ~3 mmol m^{-3} at day 10 to ~30 mmol m^{-3} at day 20, eventually approaching a value of ~70 mmol m^{-3} (Figure 2). The rise in C_{bot} is driven, ultimately, by the sinking of particles produced in the surface box, C_{top}, into the bottom box. The C_{top} response is characterized by a rapid initial rise in concentration, with C_{top} at day 10 greater than 9 mmol m^{-3}, nearly an order of magnitude higher than the initial condition (Figure 2b). By day 20, C_{top} is near the peak value of ~70 mmol m^{-3}; however, unlike the deep box dynamics, the particle evolution advances through a local minimum just after day 25, followed by a slower secondary rise toward the steady state value of ~60 mmol m^{-3}. The details of the fluctuations during this

transition from the initial growth phase toward the later asymptotically steady regime are dependent on the initial concentration values as well as the other model parameters.

The rise in C_{top} is initially sustained by the upwelling of N_{bot}, but in all cases, consumption eventually exceeds the upwelled source, and N_{top} begins to decline. As long as N_{top} remains much greater than K, so that $N_{top}/(K+ N_{top}) \approx 1$, C_{top} growth is approximately exponential at the maximal (i.e., nutrient-saturated) accumulation rate α, where

$$\alpha = p - r - s - \lambda. \tag{3.1}$$

Even as C_{top} is growing exponentially, N_{top} also initially grows, due to upwelling of the high N_{bot} waters. By day 10, for FP, N_{top} has risen to near its peak value of over 20 mmol m^{-3}. At that point C_{top} has reached such a high level that the consumption of N_{top} begins to exceed the upwelled supply, and N_{top} begins to fall, reaching a minimum of just over 1 mmol m^{-3} shortly after day 20. N_{top} then rebounds, passing through a weak local maximum of about 3 mmol m^{-3} near day 25, corresponding to the C_{top} local minimum, before settling toward the asymptotic value just under 3 mmol m^{-3}. The postminimum fluctuations are driven by the dynamics of the supply of N_{bot} to the surface (Figure 2b). Following the initially slow rise of ΔO_{bot}, N_{bot} has risen by only 0.2 mmol m^{-3} by day 10, and < 3 mmol m^{-3} by day 20, the time of the N_{top} minimum. After that, N_{bot} follows a slow rise toward an asymptotic value of $\sim$55 mmol m^{-3}. This interplay between the surface nutrient concentration evolution and the increasing contribution of bottom nutrients supplied by respiring C_{bot}, plays a large role in the evolution of oxygen depletion of the bottom shelf water.

Oxygen depletion for the SP case is strikingly distinct from the FP case. At 10- and 20 day benchmarks, ΔO_{bot} (Figure 3a; light line, Figure 2a) is < 0.02 and < 0.08 mmol m^{-3}, orders of magnitude less than seen for the FP-case. Oxygen depletion for SP never even approaches the moderate hypoxia threshold, instead asymptotically approaching only $\sim$9 mmol m^{-3}. Similar to the FP case, the SP ΔO_{bot} evolution is a fairly straightforward connection to the C_{bot} evolution: a rise that slightly lags the C_{bot} rise, with each case reaching asymptotic values with $\Delta O_{bot} \sim 3C_{bot}$.

Like the FP case, SP ΔO_{bot} dynamics are ultimately tied to production of C_{top} and sinking through the midwater column into the bottom box, but similarity ends there. Growth of C_{top} (Figure 3b) is, expectedly, slower for the slower specific growth rate p, with C_{top} at the 10 and 20 day benchmarks of only < 3 and < 7 mmol m^{-3}, 3 and 10-fold lower than FP at the corresponding times. SP C_{top} reaches its local maximum over 35 days later, and then drops and proceeds to an asymptotic condition without passing through a local minimum. The SP C_{top} dynamics are controlled similarly to the FP case: low initial C_{top} allows N_{top} to grow in response to upwelling until exponential C_{top} growth leads to N_{top} consumption exceeding upwelling supply, causing nutrients to fall to a low and nearly constant value approaching the limiting K value. However, the maximum and asymptotic C_{top} values for SP, $\sim$185 and $\sim$163 mmol m^{-3}, respectively, are each nearly 3x higher than corresponding FP values.

3.2. Oxygen Depletion and Retention Efficiency

Oxygen depletion for a given flushing or upwelling rate is determined by the overall amount of respiration of C_{bot}; this is ultimately linked to the production of C_{top} and thus the upwelling-rate dependent delivery of nutrients to the surface. This suggests that upwelling will favor hypoxia when the surface particle dynamics and export are fast enough to keep up with upwelling transports and focus that respiratory potential on the bottom box [*Bakun*, 1990; *Bakun et al*., 2015]. The latter capacity can be quantitatively characterized by the retention efficiency, c, defined here as:

$$c(t) = \frac{\int_0^t rC_{bot}dt'}{\gamma \int_0^t \lambda N_s dt'}, \tag{3.2}$$

where the numerator represents the integrated consumption of oxygen by respiration of particles in the bottom box, and the denominator measures the integrated potential for respiration from nutrient supplied to the system by upwelling, i.e., the respiration that would result from its complete transformation into respiring bottom-box particles. If rapid particle growth and sinking efficiently converts upwelled nutrients into C_{bot}, the retention efficiency c will be large and the system will rapidly lose oxygen. If slow particle growth allows potential respiration to escape offshore in the form of un-utilized nutrient, retention

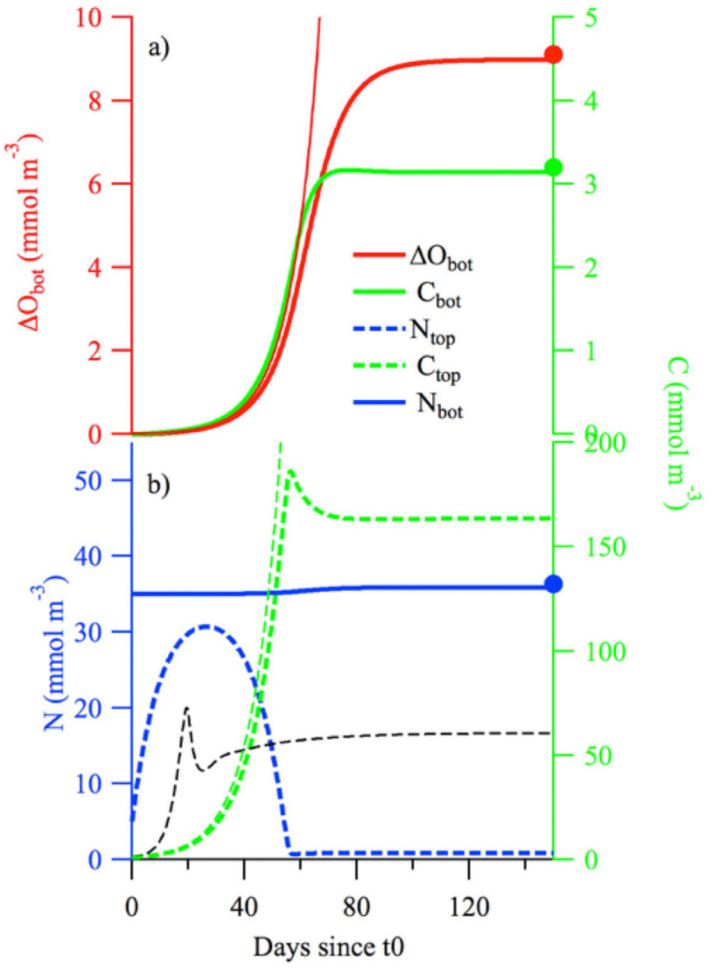

Figure 3. Temporal evolution of model with constant forcing at $\lambda = 0.1\ d^{-1}$ as in Figure 2, for the SP parameter set. (a) Evolution of the deep-box oxygen depletion and particle accumulation; and (b) evolution of the surface particle accumulation and surface and deep nutrient concentrations. Other curves are shown for comparison: the deep-box oxygen depletion predicted from the exponential approximation (light red line, Figure 3a); the C_{top} predicted from the exponential approximation (Figure 3b, light dashed green line); and the C_{top} for the FP parameter set (Figure 3b, light dashed black line; same as heavy dashed green line in Figure 2b).

efficiency and oxygen depletion will be low. Efficiency and depletion will also be low if slow sinking allows C_{top} to be transported offshore, or prevents surface export from being effectively transferred to E_{bot}.

Temporal evolution of the retention efficiency (3.2) for the FP and SP examples demonstrates its fundamental relation to ΔO_{bot} evolution (Figure 4a). The FP case shows a rapid rise in retention of the respiration potential of upwelled source water nutrients toward an asymptotic value approaching 0.5; in contrast, the SP retention never exceeds 0.02 (Figure 4a). The differences in retention in these two cases are primarily due to differences in loss of respiration potential by offshore transport. In the FP case, about half of the respiration potential has been exported offshore from the surface box, in a roughly 2:1 ratio between export of C_{top} that avoids sinking and N_{top} that has not been incorporated in net C_{top} production. In the SP case, nearly 75% of the respiration potential is lost via offshore export of C_{top} and N_{top}.

If there is a steady-state balance between respiration and flushing in (2.1), such as is approached for large times in the FP and SP cases, then by (2.10) the retention efficiency (3.2) is (with overbar indicating steady-state value)

$$c(t) = \overline{c} = \overline{N_{bot}}/N_s - 1 \ . \tag{3.3}$$

This result shows that the retention efficiency can exceed one if the bottom-box nutrient concentration is more than twice that of the source water, $N_{bot} > 2N_s$. This "super-efficiency" is possible because nutrients that are retained in the nutrient-particle-oxygen cycle within the model boxes can effectively respire multiple times, rather than just once. An efficiency normalized instead by the upwelling nutrient flux into the top box, $\int \lambda\ N_{bot} dt\prime$, can be shown never to exceed one (except for a possible transient response to large initial particle loads), but is less useful because that flux is not known a priori from the imposed upwelling rate and source-water conditions. From (A3), and (A2), it is straightforward to see that the instantaneous depletion ΔO_{bot} is no greater than $v \int_0^t \lambda N_s dt\prime$ plus a constant, so the instantaneous depletion is limited by the total time-integrated onshore nutrient transport. In steady state, however, the latter becomes infinite while the depletion remains finite; thus, the associated alternative efficiency ratio of instantaneous depletion to total onshore transport will always approach zero, and so this alternative too is less useful than (3.2). On the other hand, (A3) shows that oxygen depletion is proportional to enhancement of bottom nutrient

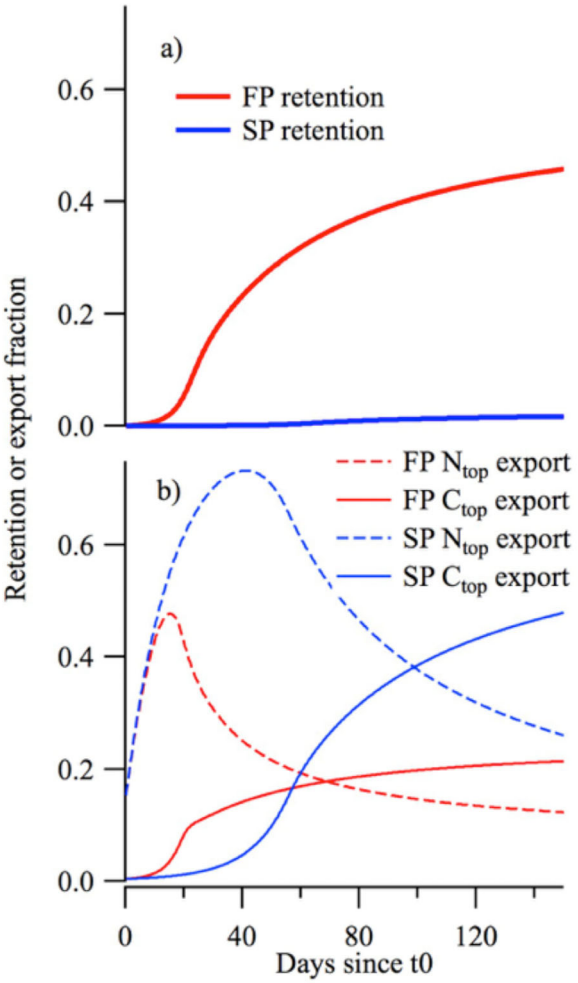

Figure 4. (a) Efficiency of retention ($c(t)$ from equation (3.2)) of respiratory potential for the FP (red) and SP (blue) cases shown above, and (b) Fractional export of respiratory potential via N (dashed lines) and C (solid lines) export from the top box.

concentration over its initial value, which (neglecting the small initial nutrients above the bottom box) can only be achieved by onshore nutrient transport.

4. Rate Controls on Depletion Amplitude and Timescale

4.1. Asymptotic Steady States

The case studies (section 3) highlight two important characteristics of the temporal evolution of the steadily-forced model system: the timescale to reach a critical ΔO_{bot} threshold, which is controlled by the initial growth phase in C_{top}, and the longer term, asymptotically steady depletion that the system eventually approaches. The asymptotic values are steady states that can be determined analytically. These steady states are, of course, idealizations; ocean upwelling systems are always subject to some temporal variability. Further, as will be shown, the model steady-state depletion can be quite large, often exceeding the oxygen concentrations not only of typical upwelling source waters, but also exceeding that in the most oxygenated ocean waters. Nonetheless, the steady states can be used to characterize the maximum potential de-oxygenation over a wide range of parameter space. This allows analysis of the system's response to key parameters, and of the factors that can drive the system to hypoxia and anoxia.

The steady states are approached when particle production eventually reaches nutrient limitation in the top box, slowing the growth of C_{top} and resulting, for a given value of s, in a constant delivery of particles to the bottom box, in turn allowing a steady-state for ΔO_{bot} that balances the flushing of the box by offshore water with consumption of oxygen by respiration of particles. Explicit expressions for these steady-state solutions can be obtained by setting the time derivatives in (2.4)–(2.8) to zero, and are given in the Appendix A (equations (A4)–(A9)). The key result is for the steady-state oxygen depletion, $\overline{\Delta O_{bot}}$:

$$\overline{\Delta O_{bot}} = F(r,s,\lambda,\delta)\ v\left(N_s - \overline{N_{top}}\right), \tag{4.1a}$$

where

$$F(r,s,\lambda,\delta) = \frac{\delta s^2}{rs + (r+s\delta)\lambda}, \tag{4.1b}$$

and,

$$N_s - \overline{N_{top}} = \left(1 - \frac{p_* K_*}{\alpha}\right) N_s = N_s - \left(\frac{p}{\alpha} - 1\right) K\ . \tag{4.1c}$$

In (4.1c), $p_* = (r+s+\lambda)/N_*$, where $K_* = K/(K+N_s) \ll 1$ and $N_* = N_s/(K+N_s) = 1 - K_* \approx 1$ are dimensionless half-saturation constant and source nutrient levels, respectively. These steady states prove always to be stable: small perturbations from them decay, so that the perturbed solution evolves back toward the steady state at the exponential rate $\lambda r(r+\delta\lambda)/[\delta s(r+\lambda)]$.

The steady-state bottom oxygen depletion $\overline{\Delta O_{bot}}$ is thus the product of two factors, with the first, F defined in (4.1b), dependent only on respiration (r), sinking (s, δ) and the physical forcing (λ). The nutrient source concentration N_s, half-saturation K, production rate p, and the stoichiometry ν appear only in the second factor, which additionally depends (through α) on r, s, and λ, but not on δ. The last expression in (4.1c) shows directly that the dependence of $\overline{\Delta O_{bot}}$ on N_s is linear, so that an increase in source-water nutrient concentrations will cause a proportional increase in steady-state bottom oxygen depletion when all other parameters are held fixed.

If the production rate p is sufficiently small that net particle growth is not supported, then $\overline{N_{top}} = N_s$, and from (4.1a) there is no bottom oxygen depletion. When the intrinsic surface particle production rate p is large enough that production of *Ctop* is supported (i.e., when p is substantially greater than p_*), further increases in p have almost no effect on bottom oxygen depletion, provided that all other system parameters – notably the sinking rate s – are held fixed (Figure 5a). Thus, in the productive regime, the primary control on steady state bottom-oxygen depletion with respect to examined variations in the model parameter space is exerted not by p but by the first factor on the right-hand side of (4.1a). This limited dependence on p can be anticipated from the second expression in (4.1c), as the first factor is nearly unity unless $\alpha \approx p_* K_*$ (i.e., unless $p \approx p_*$; see Appendix A), and $\alpha = p - r - s - \lambda$ increases linearly with p. As p decreases (or as r, s, or λ increases), the no-growth point is seen from (4.1c) to be first reached not when $\alpha = 0$, but instead when $\alpha = p_* K_*$ (or, equivalently, when $p = p_*$).

In contrast to variations in p, variations in λ and s have large effects on the steady-state oxygen depletion (4.1) even far from the corresponding critical values $\lambda_* = pN_* - r - s$ and $s_* = pN_* - r - \lambda$, where the no-growth point is again reached. When λ varies with all other parameters fixed at their values for the FP and SP particle-specific parameters (Figure 5b), the maximal oxygen depletion is found at minimal (zero) upwelling forcing, and the minimum depletion (zero) at the corresponding critical λ values for these parameter sets ($\lambda_* =$ 0.37 and 0.20 d^{-1}, respectively). This behavior is general: with s and all other parameters fixed, both factors in (4.1a) decrease monotonically with increasing λ until $\overline{\Delta O_{bot}}$ vanishes at the no-growth point, $\lambda = \lambda_*$. Thus, the maximum steady-state depletion is found as λ approaches zero, and is equal to $\overline{\Delta O_{bot}(\lambda \to 0)} = \frac{\delta s}{r} \nu \left(N_s - \frac{r+s}{p-r-s} K\right) \approx \frac{\delta s}{r} \nu N_s$. It is notable that the SP case never achieves an hypoxic steady-state depletion over the allowable range of λ, reaching a maximum of only 30 mmol m^{-3} even in the limit of zero upwelling forcing.

The approach to a maximum depletion for no upwelling ($\lambda = 0$) is a curious result, suggesting that if upwelling never occurred, the system could reach maximum oxygen depletion. This is, of course, inaccurate: an unforced system has an oxygen depletion limited by the respiration potential of the initial C_{top} and N_{top} conditions, as can be verified directly. For the steady-state solutions, however, oxygen depletion increases with decreasing upwelling all the way to the limit of zero upwelling. The resolution of this apparent inconsistency comes in the very long times necessary to achieve the steady state under infinitesimal upwelling forcing: infinitesimal upwelling produces maximal oxygen depletion, but only after infinitely long timescales.

The steady-state solutions also show a strong dependence on the sinking rate s (Figure 5c). Depletion increases with s over most of the allowable range, in accordance with the s-dependence of the first factor in (4.1a), as increasing the sinking rate enhances the export of C_{top} and reduces attenuation by respiration in the middle box. A sharp cut-off occurs for the largest allowable s, as fast sinking rates remove surface particles so rapidly that production declines and less nutrients are consumed. The minimum sinking rate is trivially 0; the maximum sinking rate, analogous to the maximum upwelling rate, comes when $s = s_*$, making the net C_{top} accumulation rate zero and extinguishing export. In between these two limits, and close to the upper limit $s = s_*$, there is an optimum value s_{opt} that maximizes oxygen depletion potential. Steady-state de-oxygenation is thus bounded by $0 < \overline{\Delta O_{bot}} < F(r, s_{opt}, \lambda, \delta)\ \nu(1 - p_* K_* / \alpha_{opt}) N_s$, where the lower limit corresponds to $s = 0$, the upper limit to $s = s_{opt}$, and $\alpha_{opt} = p - r - s_{opt} - \lambda$; an analytical expression for s_{opt} is derived below (section 5.2).

With other parameters fixed as in the FP and SP cases (Figure 5c), the optimal sinking rates s_{opt} are found near $s =$ 0.65 and 0.13 d^{-1}, respectively, close to the corresponding cut-off values, $s_* =$0.77 and 0.15 d^{-1}. The maxima around these optimal sinking rates are broad: oxygen depletions of up to half the maximum are found over roughly half the allowable ranges of s. The depletions for the FP and SP optimal sinking rates

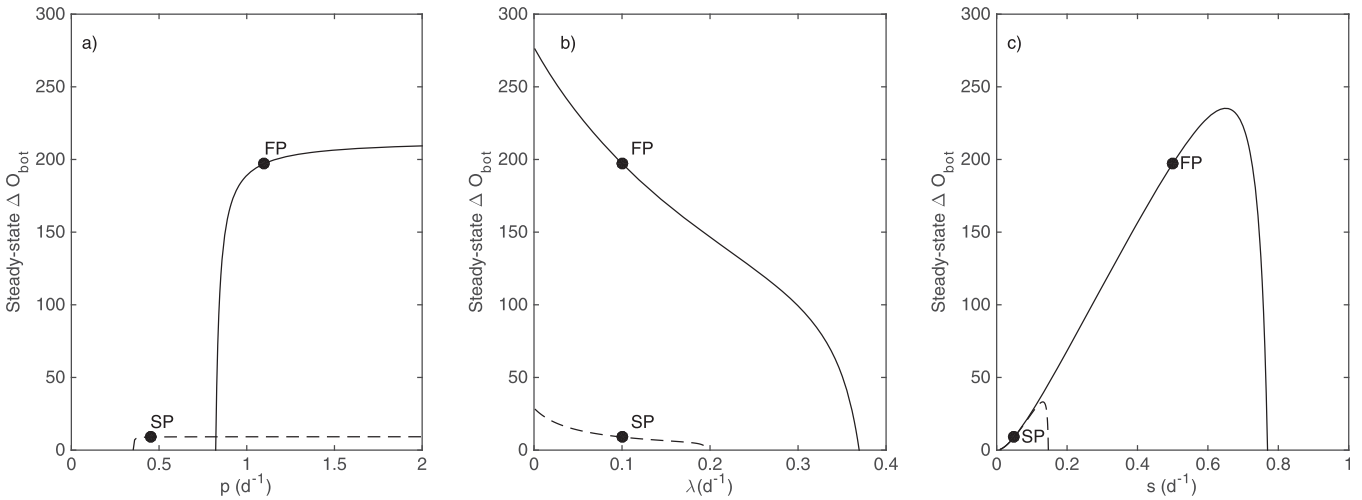

Figure 5. Steady-state oxygen depletion with other parameters as for the FP (solid line) and SP (dashed) parameter sets versus variable (a) production rate p, (b) upwelling rate λ and (c) sinking rate s. Black circles show solutions corresponding to the model results from Figures 2 and 3, with the fixed FP and SP values of p, λ and s.

are very different: with a modified, near-optimal sinking rate, FP can attain extreme hypoxia (ΔO_{bot} > 100 mmol m^{-3}), while even the optimal sinking rate for SP results in only a modest depletion (17 mmol m^{-3}). For small s, however – that is, below the cut-off value s_* for SP – the depletions are essentially identical, indicating that the different values of p and K for FP and SP have almost no effect on the relative oxygen depletion levels. Instead, it is the different values of s that control the behavior; the larger p value for FP is important as a driver of potential hypoxia only insofar as it allows larger values of s without extinguishing surface productivity.

4.2. Timescales to Hypoxia

As noted above, the initial surface particle response is largely not nutrient-limited, and approximately follows an exponential growth trajectory until N_{top} is sufficiently depleted to limit C_{top} growth. Since oxygen depletion is driven by respiration of particles in the bottom box, which are ultimately supplied by the export of particles from the top box, the exponential rise in C_{top} has direct bearing on the initial rate of depletion. For this exponential growth phase, the model surface-box C_{top} has an approximate analytical solution given by:

$$C_{top}(t) \approx C_{top,0} e^{\alpha t} \tag{4.2}$$

This shows the leading dependence of the initial response on the model parameters in the form of the previously defined maximal accumulation rate $\alpha = p\text{-}r\text{-}s\text{-}\lambda$.

The exponential approximation yields reasonable agreement with the full solution for C_{top}, within a factor of two for the FP case for $\sim$ 10 days, and within a factor of 1.5 for the SP case all the way to the C_{top} maximum at 56 days (Figures 2b and 3b), but the greater relevance is to the initial rise in ΔO_{bot}. The existence of the approximate analytical solution (4.2) for *Ctop* while *Ntop* $\gg$ *K* leads to a similar approximation for ΔO_{bot}:

$$\Delta O_{bot}(t) \approx \frac{\nu C_{top0}}{\gamma G(r,s,\lambda,\delta)} e^{\alpha t}, \tag{4.3}$$

In (4.3), the function G is

$$G(r,s,\lambda,\delta) = \frac{(\alpha+\lambda)(\alpha+r)(\alpha+r+\delta s)}{r\delta s^2} \tag{4.4}$$

and captures the factors that ultimately link export of C_{top} with input to, and respiration in, the bottom box. Comparison of the full solution for ΔO_{bot} with the exponential approximations shows remarkable adherence for a surprisingly long time: For the FP case, the exponential approximation is within a factor of two of the full solution for 15 days (Figure 2a), while for the SP case the agreement is within 20% of the smaller ΔO_{bot}

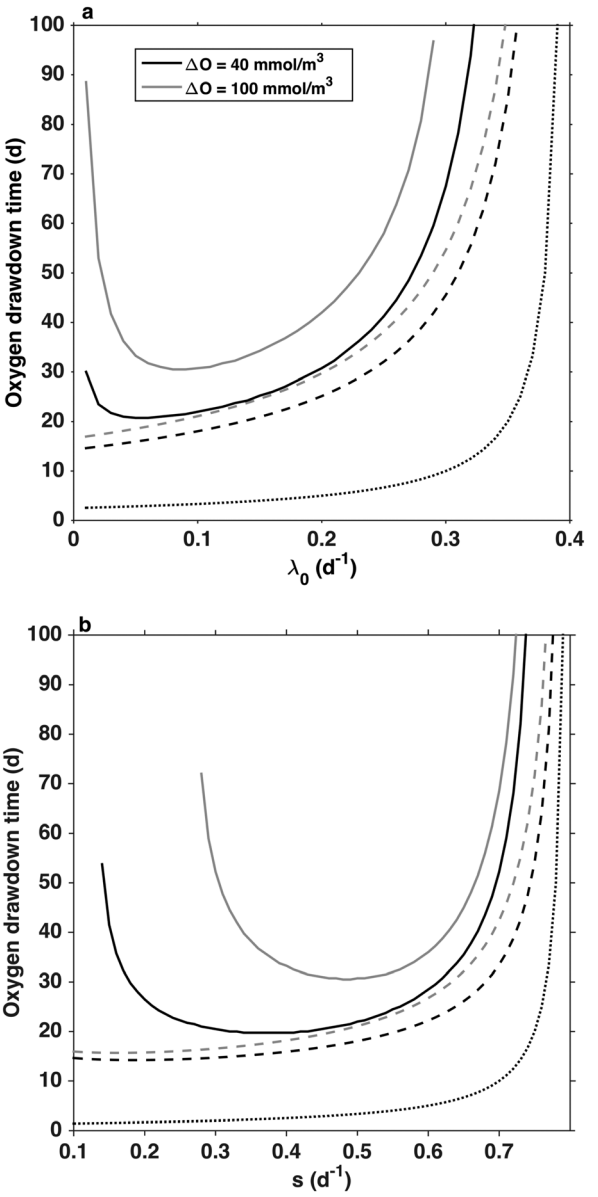

Figure 6. Timescales for oxygen depletion versus (a) λ and (b) s for other parameters fixed at their FP-case values. Light and heavy solid lines show the times for the full model to reach $\Delta O_{bot} = 100$ and 40 mmol m^{-3}, respectively, while the corresponding dashed lines show the same timescales for the exponential approximations. The light dotted line shows the characteristic surface exponential-growth time, α^{-1}.

for over 50 days (Figure 3a). In the FP case, where hypoxic thresholds are achieved, the exponential approximation finds moderate hypoxia ($\Delta O_{bot} = 40$ mmol m^{-3}) at 18 days, just 4 days before that condition is attained by the full model, suggesting a strong predictive capability for the onset of hypoxic conditions using this simplified approximation and knowledge of a handful of inherent system timescales. Predictions beyond that point are worse but still meaningful, with the exponential approximation predicting extreme hypoxia in 21 days, while the full solution requires 31 days to reach that state ($\Delta O_{bot} = 100$ mmol m^{-3}).

Equation (4.3) can be rearranged to solve for the time t_{hyp} at which a specific value of ΔO_{bot}, ΔO_{hyp}, is reached:

$$t_{hyp} \approx \frac{1}{\alpha} \ln\left(\frac{\gamma \Delta O_{hyp}}{\nu C_{top0}} G\right) . \qquad (4.5)$$

As the SP case never results in appreciable oxygen depletion, the timescales to hypoxia for the exponential approximations and the full numerical solutions are compared for varying λ (Figure 6a) and s (Figure 6b) only for the nominal FP case with the fast growth rate (large p). The full solutions predict broad minima of <30 days for $\Delta O_{bot} = 40$ mmol m^{-3}, for $0.02 < \lambda < 0.2$ (flushing timescale of 50–5 days) with such conditions reached in as little as 20 days for $\lambda \sim 0.04$, or a flushing timescale of 20 days. The times to reach extreme oxygen depletion ($\Delta O_{bot} = 100$ mmol m^{-3}) are correspondingly greater, with this condition being reached within 40 days for 0.04 d$^{-1} < \lambda < 0.15$ d^{-1} (25 – 7 d flushing timescale), with a fastest attainment of 30 days at $\lambda \sim 0.08$ (12 day upwelling timescale). Sensitivity to s shows qualitatively similar patterns: There are broad minima in the attainment of $\Delta O_{bot} = 40$ mmol m^{-3} (<30 days for 0.2 d$^{-1} < s < 0.6$ d^{-1}, with a minimum of 20 d for $s \sim 0.4$ d^{-1}) and $\Delta O_{bot} = 100$ mmol m^{-3} (< 40 days for 0.35 d$^{-1} < s < 0.6$ d^{-1}, with a minimum of 30 days for $s \sim 0.35$ d^{-1}). Outside of these respective minima, the timescales for achieving significant oxygen depletion increase rapidly, suggesting that outside of these parameter bounds there is limited capacity for achievement of hypoxia within an upwelling season, regardless of the asymptotic potential oxygen depletion.

The exponential approximations provide reasonable estimates of the full-solution timescales within these broad minima, although they are consistently lower. For the $\Delta O_{bot} = 40$ mmol m^{-3} case, the exponential approximation (4.5) yields timescales that are within 75% of those predicted from the full model, and within 60% for that minimum for the $\Delta O_{bot} = 100$ mmol m^{-3} case. For varying s, the comparison is slightly worse, with exponential approximations as low as 50% of the full model solution for the 40 mmol m^{-3} case and

40% for the 100 mmol m^{-3} case. Nonetheless, the exponential approximations give predictions that are mostly within a factor of two, and often much better, of the timescales of bottom oxygen depletion for wide ranges of parameter space.

4.3. Control by Production and Sinking Rates: A Combined Perspective

For a given set of model parameters, the timescale (4.5) for approach to hypoxia is only relevant if the steady-state depletion (4.1) is large enough to make the system potentially susceptible to hypoxia. If the steady state depletion (4.1) is sufficient to cause hypoxia, then the exponential approximation (4.5) will provide an estimate of the timescale to reach hypoxia that is accurate enough to evaluate, for example, whether hypoxia might be reached within an upwelling season. If, on the other hand, the steady state depletion is not sufficient to cause hypoxia, then the timescale estimate (4.5) does not apply, because the system will never reach hypoxia. The steady-state depletion (4.1) depends strongly on sinking rate s, but is nearly independent of production rate p as long as a threshold rate for growth is exceeded (Figure 5). In contrast, the estimated timescale to hypoxia (4.5) depends strongly on p and only weakly on s (Figure 6). A combined perspective on the susceptibility of the model system to hypoxia can be developed by considering the dependence of these two metrics jointly on p and s, with other parameters held fixed.

The combined perspective can be efficiently described, or assisted, by a single contour plot of the depletion (4.1) and timescale (4.5) versus p and s (Figure 7), which shows only the relevant one of these two quantities in each sector of the plot: only the timescale, if the steady-state depletion is hypoxic, and only the steady-state depletion, if this depletion is not hypoxic. Thus, for a given hypoxic threshold ΔO_{hyp} (chosen for Figure 7 as the extreme value 100 mmol m^{-3}, corresponding to anoxia when $O_s = 100$ mmol m^{-3}), contours of the exponential timescale (4.5) are drawn where the steady state depletion (4.1) exceeds ΔO_{hyp}, while contours of the depletion (4.1) itself are drawn where its value does not exceed ΔO_{hyp}. The resulting combined contour plots show more generally, for a broad range of p and s values, that the ultimate capacity for oxygen depletion is mostly dependent on s, and is essentially independent of p values, except near the critical line $s = s_* \ (\alpha = pK_*)$. In contrast, the timescales for attaining hypoxic states are mostly sensitive to p, and are nearly independent of s.

The similarity of these representations for the FP (Figure 7a) and SP (Figure 7b) values of K shows additionally that the difference in K has negligible effect on the potential for oxygen depletion. The ultimate development of hypoxia is thus entirely driven by coincidence of two fast rates: high sinking rates ($s > 0.3$ d^{-1}) are required for development of consequential hypoxia, while high surface production rates (p greater than the critical value α/K_*) are required for that development to take place on reasonable timescales relative to an upwelling season.

5. Generalized Analysis of Susceptibility to Hypoxia

5.1. Relative-Rate Scaling

Even in this highly simplified model, the number of free parameters is large enough to confound a complete characterization of the oxygen depletion response as a function of all model parameters. However, substantial progress toward this goal is possible. For a given system, the combined analysis of steady-state depletion and exponential timescale developed above (section 4.3, Figure 7) provides a relatively complete description of the susceptibility to hypoxia for all plausible values of p and s. Further, the steady-state depletion (4.1) was seen to be linearly dependent on N_s, while the timescale to hypoxia, approximated following (4.5) under the assumption $N_s \gg K$, is independent of N_s.

A first step toward a more general characterization follows from the recognition that the steady-state depletion (4.1) depends only on the dimensionless ratios of the fundamental rates, not their absolute, dimensional values. Consequently, choosing one rate to define a master timescale, and normalizing the others by that master rate can remove one free parameter. The sum of the respiration and upwelling rates, $r + \lambda$, describes the nonsinking fraction of surface particle loss, and proves to be a convenient choice for the master rate. With this choice, the normalized particle production, sinking, and maximal accumulation rates are

$$(\tilde{p}, \tilde{s}, \tilde{\alpha}) = (p, s, \alpha)/(r+\lambda), \tag{5.1}$$

where $\tilde{\alpha} = \tilde{p} - 1 - \tilde{s}$, and the normalized sinking rate $\tilde{s}$ represents the ratio of sinking to nonsinking fractions of surface particle loss. The steady-state depletion (4.1) can then be written as,

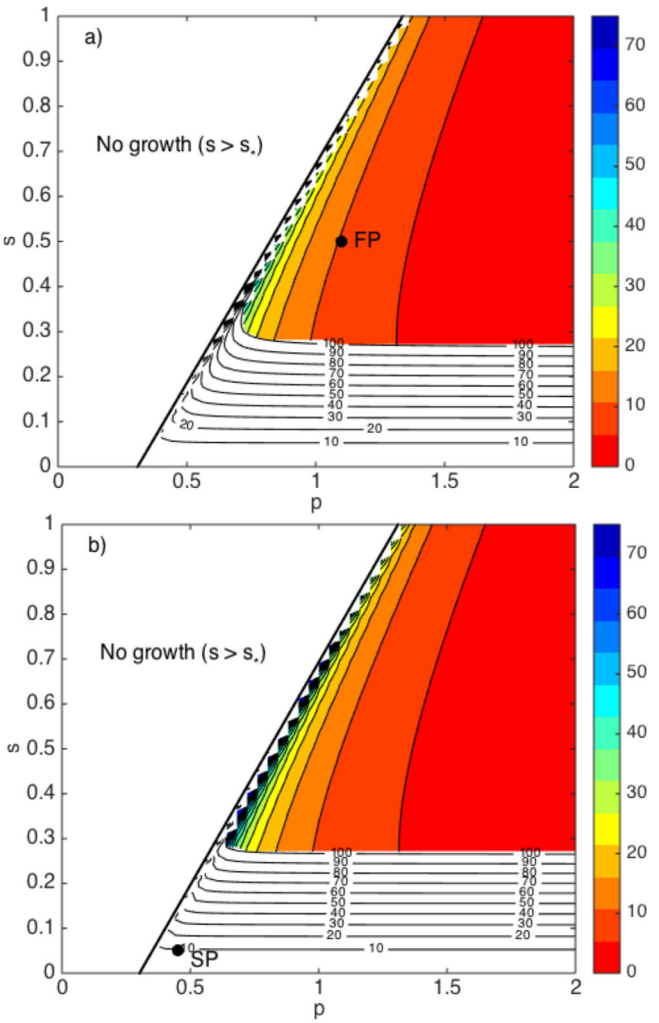

Figure 7. Combined contour plot of steady-state depletion and timescale metrics versus dimensional productivity and sinking rates, p and s (d^{-1}), for a hypoxic threshold value $\Delta O_{hyp} = 100$ mmol m^{-3} and the (a) FP and (b) SP values of all other parameters. Steady state bottom-oxygen depletion ΔO_{bot} (mmol m^{-3}; labeled line contours) is shown where it is less than ΔO_{hyp}. Estimated time to hypoxia t_{hyp} (d; color-filled contours) is shown where the steady-state depletion is greater than ΔO_{hyp}. Other parameter values are: $(r,\lambda) = (0.2,0.1)$ d^{-1}, $\delta = 1/3$, $N_s = 35$ mmol m^{-3} and (a) $K = 1$, (b) $K = 0.25$ mmol m^{-3}. The FP and SP values of (p,s) are indicated (black dots). The critical lines $s = s_* = pN_* - r - \lambda$ are also shown (solid); for $s > s_*$, there is no growth or retention ($C_{top} = C_{bot} = \Delta O_{bot} = 0$).

$$\overline{\Delta O_{bot}} = \hat{F}(\tilde{s}, \delta, \Lambda)\ v\left[N_s + \left(1 - \frac{\tilde{p}}{\tilde{\alpha}}\right)K\right], \tag{5.2a}$$

where

$$\hat{F}(\tilde{s}, \delta, \Lambda) = \frac{\delta(1+\Lambda)^2\tilde{s}^2}{\Lambda + (1+\Lambda)(1+\delta\Lambda)\tilde{s}}, \tag{5.2b}$$

and

$$\Lambda = \lambda/r \tag{5.2c}$$

is the ratio of upwelling rate to respiration rate. Thus, $\overline{\Delta O_{bot}}$ is seen from (5.2) to depend on only three dimensionless, relative rate parameters – $\tilde{s}$, Λ, and $\tilde{p}$ – rather than the four dimensional rate parameters p, r, s, and λ in (4.1). Similarly, the scaled exponential depletion timescale $\tilde{t}_{hyp} = (r+\lambda)\ t_{hyp}$ can be seen from (4.4)–(4.5) also to be a function only of the relative rates.

This reduction to dependence on relative rates means that, when other parameters are fixed, the system response (including the dimensionless timescale $\tilde{t}_{hyp}$) is unchanged if the dimensional production, sinking, respiration, and upwelling rates are all increased or decreased by the same factor. Note that this implies that the dimensional timescale $t_{hyp} = \tilde{t}_{hyp}/(r+\lambda)$ is changed by the inverse of that same factor: if all rates were doubled, for example, the steady-state depletion would be unchanged, but the dimensional timescale t_{hyp} would decrease by half.

When the combined depletion and timescale analysis (section 4.3, Figure 7) is recast and expressed in terms of the relative production and sinking rates, $\tilde{p}$ and $\tilde{s}$, it is seen to apply much more generally to all systems with the same values of these relative rates, rather than only for a single value of r and a single value of λ (such as the FP and SP values $r = 0.2$ d^{-1}, $\lambda = 0.1$ d^{-1}, for Figure 7). The system dependence on K is more evident if the relative maximal accumulation rate $\tilde{\alpha} = \tilde{p} - 1 - \tilde{s}$ is used in place of $\tilde{p}$ in this context (Figure 8). This description in terms of the relative rate parameters $\tilde{\alpha}$ and $\tilde{s}$ is valid for all systems that have the same ratio of upwelling to respiration rates (fixed $\Lambda = \lambda/r$) and, of course, the same values of the other relevant fixed parameters (δ , K, N_s, and, for t_{hyp}, the initial surface particle concentration C_{top0} and depletion threshold ΔO_{hyp}).

It was seen above (Figure 7) that, when other parameters are fixed as in the FP or SP examples, the system was susceptible to hypoxia (or even anoxia) when $s > 0.3$ d^{-1}. The relative-rate analysis shows that this criterion corresponds more broadly to a dimensionless sinking rate $\tilde{s} > 1$ (Figure 8): setting $\tilde{s} = 1$ in (5.2), with $\delta = 1/3$ and $\Lambda = 1/2$ as in FP or SP, gives (above the productivity threshold, i.e., for $p > p_*$)

$$\overline{\Delta O_{bot}(\tilde{s}=1)} \approx \delta v N_s \approx 117 \text{ mmol m}^{-3}. \quad (5.3)$$

Similar steady-state depletions will be obtained for similar values of δ and Λ, with the analytical approximation (5.3) holding whenever $\delta \approx \Lambda/(1+\Lambda)$ and Λ is not too large. This result, like that for $\overline{\Delta O_{bot}(\lambda \to 0)}$ in section 4.1, also shows the potentially strong effect of variations in the parameter δ.

An important general conclusion thus follows from this relative-rate analysis: with Λ and other parameters fixed as in the FP or SP examples, the system will be susceptible to hypoxia whenever the sinking rate is comparable to or greater than the sum of the respiration and upwelling rates ($\tilde{s} \geq 1$, so that at least half of the surface loss is to sinking), provided also that the production rate is sufficiently large to support growth at the given sinking rate. If, on the other hand, the sinking rate is much smaller than the sum of the respiration and upwelling rates (as in the SP example with the SP value of sinking rate $s = 0.05$ d^{-1} $\ll r + \lambda = 0.3$ d^{-1}), then the system can never reach anoxia, even for arbitrarily long upwelling seasons.

Typically, the dimensionless exponential timescale $\tilde{t}_{hyp} < 10$ for $\tilde{\alpha} < 0.25$ (Figure 8), implying that if the dimensional maximal accumulation rate $\alpha = p - r - s - \lambda$ is at least one-fourth the sum $r+\lambda$ of the respiration and upwelling rates, the dimensional time to hypoxia will be of order $10/(r+\lambda)$ d or less. The latter will in turn be less than 100 d if the sum of the respiration and upwelling rates is greater than 0.1 d^{-1},. This implies that hypoxia can be reached within the upwelling season even with relatively small maximal accumulation rates that lead to little C_{top} accumulation (e.g., for $\alpha \approx 0.03$ d^{-1}), if sinking rates are large enough.

5.2. Hypoxic-Optimal Sinking

Even after the relative-rate scaling (section 5.1), the summary results (e.g., Figure 8) still depend on several potentially important parameters, especially δ, Λ and K or K_*, all of which must be held fixed for that analysis. It was seen in the FP and SP examples that the steady-state oxygen depletion, over much of the range of allowable values of sinking rate s, could be roughly characterized by the depletion at the optimal sinking rate s_{opt}, for which depletion is maximized (section 4.1, Figure 5b): the depletion is generally half or more of the maximal value over roughly half of the full range $0 < s < s_*$ of sinking rates that support particle concentration growth. For example, when s is varied while other parameters are held fixed as in the FP and SP cases, depletions of over 100 mmol m^{-3} and over 15 mmol m^{-3}, respectively, roughly half the corresponding maximal values, are obtained throughout the respective ranges $0.25 < s < 0.75$ and $0.06 < s < 0.13$ (Figure 5b). Restricting attention to this hypoxic-optimal sinking rate, and to the depletion at this rate, removes the dependence on sinking rate and thereby again reduces the number of free model parameters by one.

The hypoxic-optimal sinking-rate definition may be further generalized by using the approach in section 5.1 to obtain its dimensionless relative-rate equivalent, $\tilde{s}_{opt} = s_{opt}/(r+\lambda)$. Both this scaled sinking rate $\tilde{s}_{opt}$ (Figure 9a) and the corresponding maximal accumulation rate $\tilde{\alpha}_{opt} = \tilde{p} - 1 - \tilde{s}_{opt}$ (Figure 9b) increase monotonically with $\tilde{p}$ for any value of K_*. The dependencies of $\tilde{s}_{opt}$ and $\tilde{\alpha}_{opt}$ on K_* are opposite, with the former (Figure 9a) decreasing and the latter (Figure 9b) increasing with K_*. Thus, a system with smaller K_* will support a larger optimal sinking rate, at a smaller corresponding maximal accumulation rate, than an otherwise identical system with larger K_*. The primary dependence revealed by this analysis, however, is the indirect control of oxygen depletion potential by the production rate p (or $\tilde{p}$), through its effect on allowable sinking rates. The near linear increase of $\tilde{s}_{opt}$ with $\tilde{p}$ (Figure 9a) illustrates again the primary role that intrinsic productivity plays in controlling the system's susceptibility to hypoxia: it sets the maximum sinking velocity that can be supported without shutting down production.

An accurate analytical approximation is available for s_{opt} as a function of production rate p (see Appendix A). In relative-rate form, this analytical approximation is

$$\tilde{s}_{opt} \approx \tilde{s}_{\max}\left[1 - (\tilde{p}K_*/\tilde{s}_{\max})^{1/2}\right] = \tilde{p} - 1 - [(\tilde{p}-1)\tilde{p}K_*]^{1/2}, \quad (5.4)$$

where $\tilde{s}_{\max} = \tilde{p} - 1$ is the sinking rate for which the maximal accumulation rate vanishes (i.e., for which $\tilde{\alpha} = 0$). Remarkably, the approximate optimal sinking rate (5.4) depends only on $\tilde{p}$ and K_*, and is independent of all other parameters, including δ and Λ. The corresponding relative maximal accumulation rate, which the system would exhibit for sinking at the optimal rate, is

$$\tilde{\alpha}_{opt} = \tilde{p} - 1 - \tilde{s}_{opt} = [(\tilde{p}-1)\tilde{p}K_*]^{1/2} \quad . \tag{5.5}$$

In general, $K_* \ll 1$, so the optimal sinking rate (5.4) is always close to $\tilde{s}_{max}$, the upper bound for net surface accumulation.

5.3. Dependence on δ and Λ

As anticipated (section 4.1), the optimal sinking rate $\tilde{s}_{opt}$ from (5.4) can be substituted into (4.1) to obtain the corresponding maximal steady-state oxygen depletion $\overline{\Delta O_{bot}(\tilde{s}_{opt})}$ that is possible for given values of $\tilde{p}$, K_*, and the other fixed parameters. With the dependence on s removed in this way, attention can be focused on the dependence of the steady-state response on the previously fixed sinking-rate and upwelling-to-respiration-rate ratios, δ and Λ.

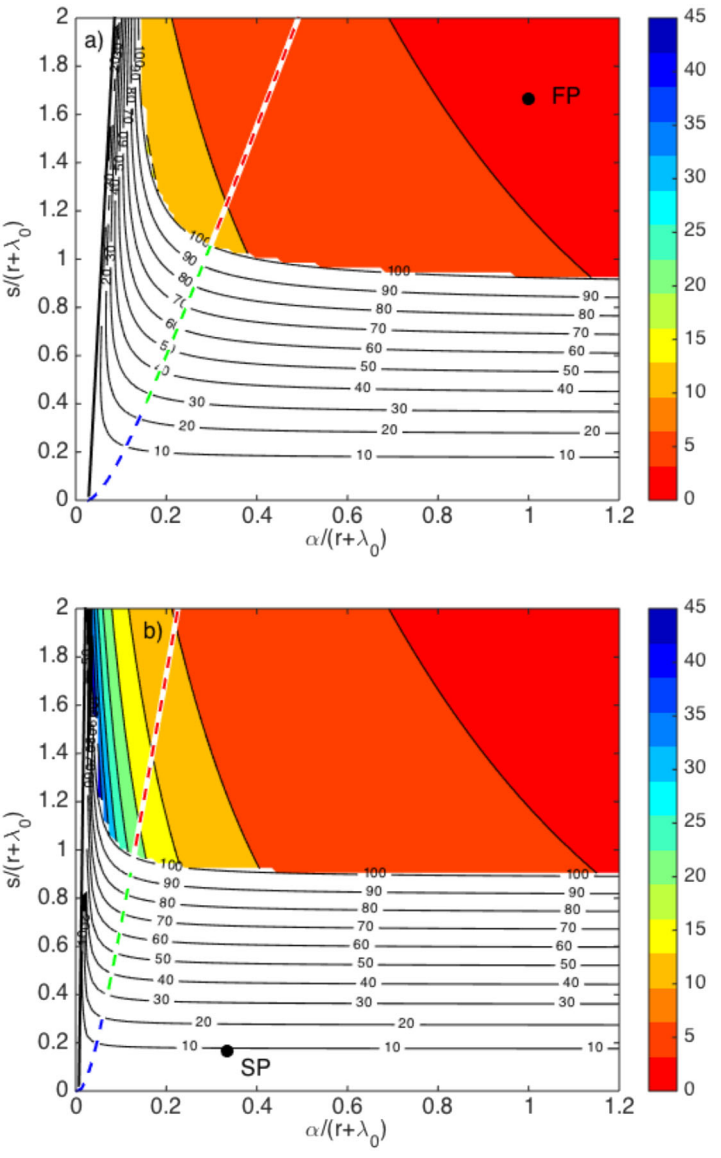

Figure 8. Combined contour plots as in Figure 7, but versus dimensionless, relative maximal accumulation and sinking rates, $\tilde{\alpha}$ and $\tilde{s}$. . Steady state bottom-oxygen depletion ΔO_{bot} (mmol m^{-3}; labeled line contours) is shown where it is less than ΔO_{hyp} = 100 mmol m^{-3}. Estimated dimensionless time to hypoxia $\tilde{t}_{hyp} = (r+\lambda)t_{hyp}$ (d; color-filled contours) is shown where the steady-state depletion is greater than ΔO_{hyp}. Other parameters are: N_s =35 mmol m^{-3}, (δ,Λ) = (1/3,0.5) and (a) K_* = 0.028 (K = 1 mmol m^{-3}), (b) K_* = 0.007 (K = 0.25 mmol m^{-3}). The FP and SP values of $(\tilde{\alpha}, \tilde{s})$ are indicated (black dots). The critical lines $\tilde{s} = \tilde{s}_*$ (solid) and $\tilde{s} = \tilde{s}_{opt}$ (dashed; blue: $\tilde{\alpha} < P_{\tilde{\alpha}}$, green: $P_{\tilde{\alpha}} < \tilde{\alpha} < P'_{\tilde{\alpha}}$, red: $\tilde{\alpha} > P'_{\tilde{\alpha}}$) are also shown. The dimensionless time $\tilde{t}$=45 corresponds to 150 d for the FP and SP value of $r + \lambda$ = 0.3 d^{-1}.

For the FP values of $\tilde{p}$ and K_*, specific-sinking-rate ratios $\delta > 0.5$ give uniformly large steady-state oxygen depletions $\overline{\Delta O_{bot}(\tilde{s}_{opt})}$, for a wide range of upwelling to respiration rate ratios Λ, while small optimal-sinking oxygen depletions are obtained only for small δ (Figure 10a). The corresponding exponential timescales are all short, and shorter for small Λ than for large Λ (Figure 11a). For the SP values of $\tilde{p}$ and K_*, ratios $\delta > 1.0$ give potentially anoxic steady-state depletions, especially for small Λ (Figure 10b). Thus, in principle, the SP values could support hypoxia for a thin middle box ($H_{mid} \leq H$) or rapid deep sinking ($S' \gg S$). However, the corresponding exponential timescales (Figure 11b) are all relatively long ($\tilde{t}_{hyp} > 45$); for $r + \lambda = 0.3$ d^{-1}, for example, the dimensional timescales are longer than the nominal 150-day upwelling season length. The overall differences in these maximal FP and SP depletions are primarily the result of the different values of $\tilde{p}$, not K_*, for the two cases.

5.4. General Criteria for Hypoxic Susceptibility

For the steady states, which provide a basic characterization of the system's potential susceptibility to hypoxia, the relative-rate and optimal-sinking analyses

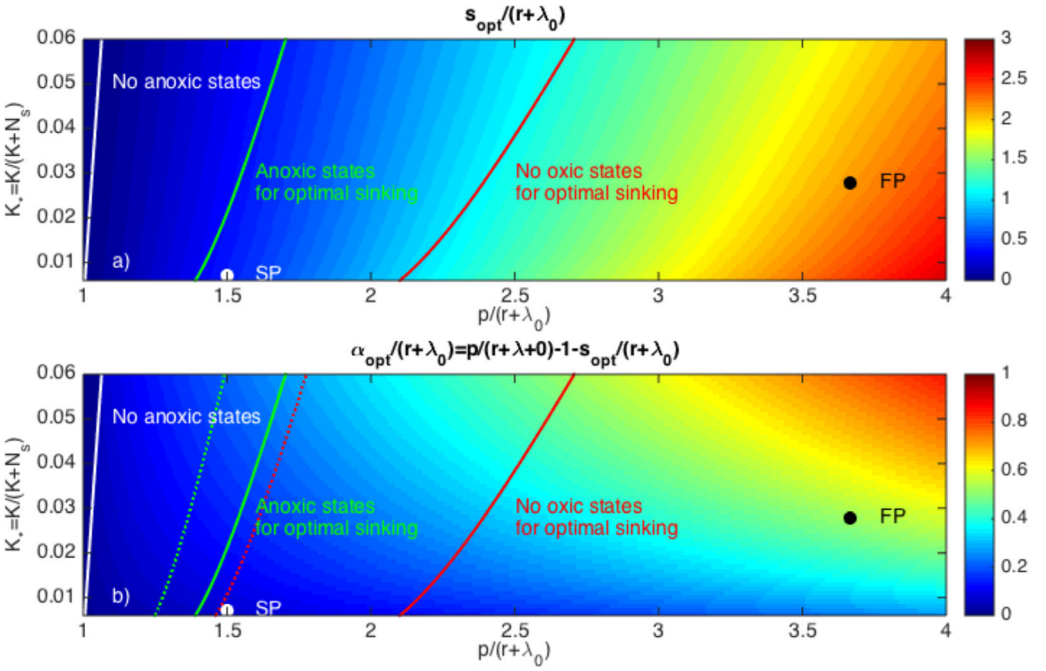

Figure 9. Optimal (a) dimensionless sinking rate $\tilde{s}_{opt}$ and (b) dimensionless maximal accumulation rate $\tilde{\alpha}_{opt}=\tilde{p}-1-\tilde{s}_{opt}$ versus $(\tilde{p},K_*)$. In both, the FP (black dot) and SP (white dot) values of $(\tilde{p},K_*)$ are indicated. The hypoxia criteria $\tilde{p}=P$ (green solid line) and $\tilde{p}=P'$ (red solid line) are shown and the corresponding regimes are indicated (white, green, red labels) for $\delta=1/3$. In Figure 9b, the criteria are also shown for $\delta=5/3$ (dotted green, dotted red).

effectively remove two of the six independent parameters that remain after the proportionality of the steady-state depletion $\overline{\Delta O_{bot}}$ to N_s is recognized, leaving the four parameters $\tilde{p}$, δ, Λ and K_*. If the dependence of the maximal oxygen depletion $\overline{\Delta O_{bot}(\tilde{s}_{opt})}$ on Λ is then examined, two simple criteria on $\tilde{p}$ emerge that broadly express the susceptibility to hypoxia as functions of the two remaining parameters, δ and K_*. Because each of these criteria depend on only two parameters, the dependence of each can be completely described by a single contour plot (Figure 12). The result is a compact and comprehensive description of the intrinsic susceptibility to hypoxia of the full model system, which assumes only that the steady-state bottom-oxygen depletion may be characterized by that obtained at the optimal sinking rate, or, equivalently, that the model sinking rate is of the same order as the optimal rate. The question of timescale to attain hypoxia is not addressed by this analysis and must be considered separately.

The criteria on $\tilde{p}$ show that the susceptibility to hypoxia depends (see Appendix A) on the values of two constants, $P(\delta,K_*)$ and $P'(\delta,K_*)$, relative to the dimensionless production rate $\tilde{p}$, which as seen before is just the ratio of the dimensional production rate to the sum of the dimensional respiration and upwelling rates. For a given value ΔO_{hyp} that is specified as the hypoxic level, these constants divide the steady-state response into three regimes (Figure 9): if $\tilde{p}<P$, then the system will never be hypoxic; if $P<\tilde{p}<P'$, then hypoxic steady states can occur for some sinking rates and some values of the ratio $\Lambda=\lambda/r$ of upwelling and respiration timescales; and if $\tilde{p}>P'$, then all steady states with normalized sinking rate equal to the optimal rate $\tilde{s}_{opt}$ are hypoxic, regardless of the value of Λ. These criteria may be expressed also in terms of the corresponding critical values $P_{\tilde{\alpha}}(\delta,K_*)$ and $P'_{\tilde{\alpha}}(\delta,K_*)$ of $\tilde{\alpha}$, where the latter are obtained by substituting P and P', respectively, for $\tilde{p}$ in (5.5).

The form of these criteria indicate that the potential for large steady-state oxygen depletion is greater for systems with relatively rapid production (large p) and relatively slow respiration and upwelling (small r and λ), which will in turn yield relatively large normalized production rates $\tilde{p}$ that will be more likely to satisfy the inequalities $\tilde{p}>P$ and $\tilde{p}>P'$. This may appear to contradict the previous results (e.g., Figures 5a, 7, and 8) that showed the relative unimportance of the production rate p for the steady-state depletion, which was seen instead to depend strongly on the sinking rate s. The apparent paradox arises from the assumption of optimal sinking (5.4) that is used to derive the criteria. This assumption effectively couples the

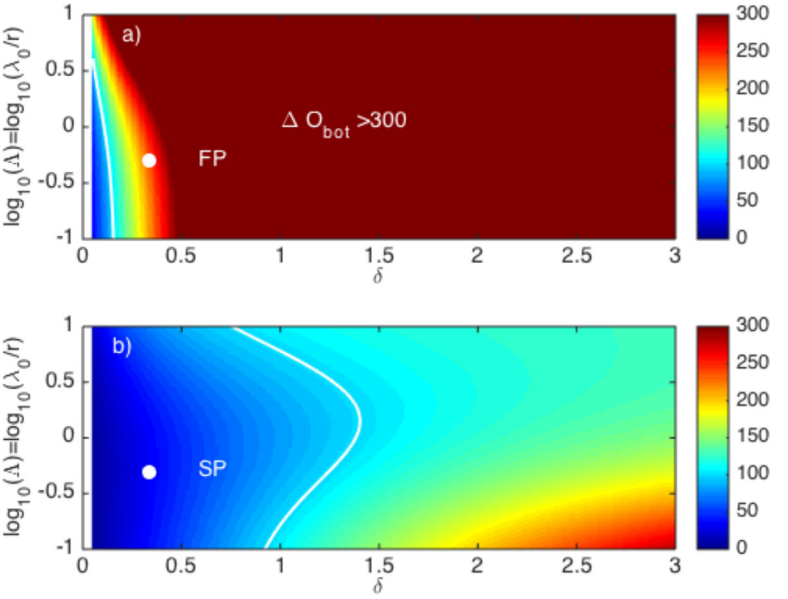

Figure 10. Steady-state oxygen drawdown ΔO_{bot} (mmol m^{-3}) at the optimal sinking rate $\tilde{s}_{opt}$ versus (δ, $\log_{10}\Lambda$), with $\tilde{p}$ and K as for the (a) FP and (b) SP examples. The 100 mmol m^{-3} contour (white) and the (a) FP and (b) SP values (white dot) of (δ, $\log_{10}\Lambda$) are indicated.

production and sinking rates, so that a larger sinking rate is implicitly associated with a larger production rate. Under this assumption, the previous indirect role of the production rate, which was found to be important only insofar as larger values allowed larger sinking rates without shutting down production, becomes a direct, controlling role.

For ΔO_{hyp} = 100 mmol m^{-3}, the values of (P, P') are (1.54, 2.39) for FP and (1.40, 2.12) for SP, while the values of $\tilde{p}$ are 3.67 for FP and 1.50 for SP. Thus, the stricter inequality ($\tilde{p} > P'$) is easily satisfied for the FP values, while the weaker inequality ($\tilde{p} > P$) is only narrowly satisfied for the SP values (Figure 9). Although neither the SP nor the FP value of the sinking rate s is equal to the corresponding optimal rate $\tilde{s}_{opt}$, it can nonetheless be anticipated

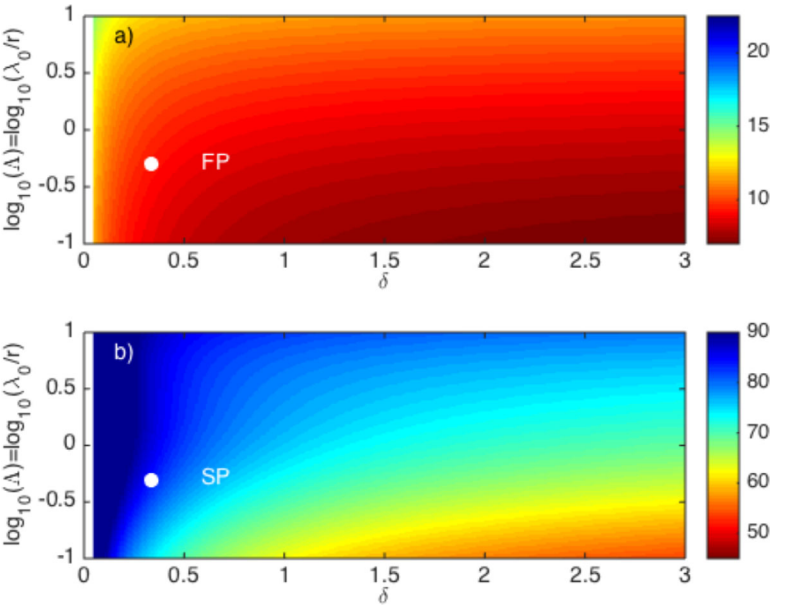

Figure 11. Exponential drawdown timescale $\tilde{t}_{hyp}$ at the optimal sinking rate $\tilde{s}_{opt}$ versus (δ, $\log_{10}\Lambda$), with $\tilde{p}$ and K as for the (a) FP and (b) SP examples. The (a) FP and (b) SP values of (δ, $\log_{10}\Lambda$) are indicated (white dots). For the FP and SP value $r+\lambda = 0.3$ d^{-1}, a nominal upwelling season length of 150 d corresponds to a dimensionless time $\tilde{t} = 45$.

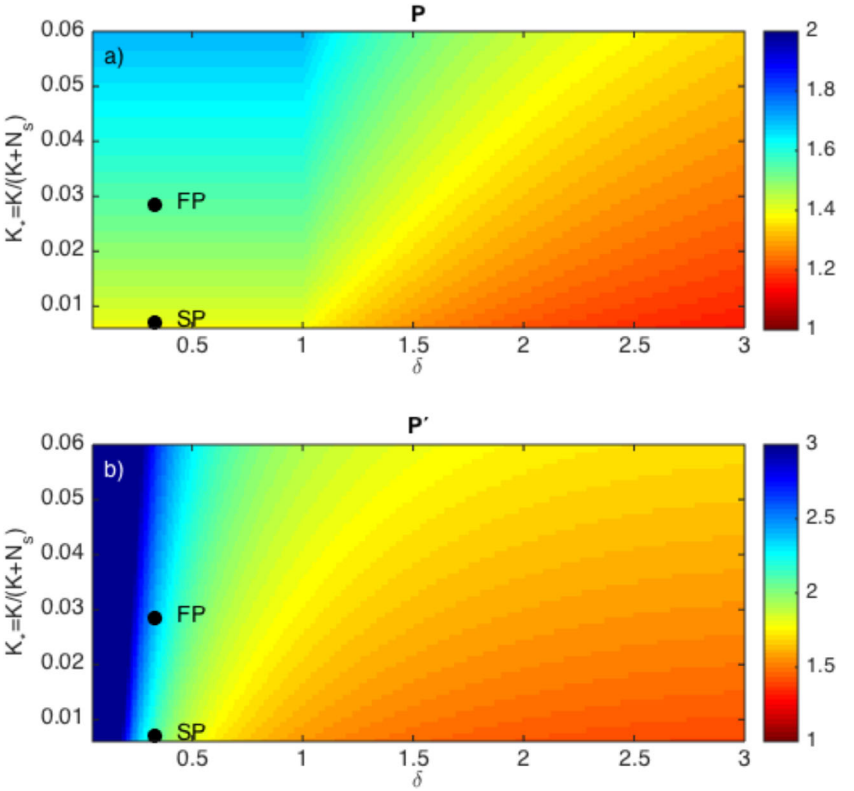

Figure 12. Steady-state hypoxia-criteria constants (a) P and (b) P' versus (δ,K_*). The FP and SP values of (δ,K_*) are indicated (black dots).

from these inequalities that the steady-state depletion for FP is likely to be sufficient to produce an anoxic steady state (for $Os = 100$ mmol m^{-3}), while that for SP is much less likely to be sufficient to produce anoxia.

Consideration of the dependence of P and P'on δ and K_* yields, finally, the desired comprehensive description of the hypoxic susceptibility of the full model system, based on the steady states and under the relatively weak condition that the source-water nutrient concentration N_s is fixed. In general, the potential for hypoxia increases as the constants P and P' decrease toward unity, reducing the value of $\tilde{p}$ that would be needed to satisfy the corresponding inequalities. The minimal value of $\tilde{p}$ for steady-state growth is $\tilde{p}=\tilde{p}_*=1/N_* \approx 1$, so when $P=1$ or $P'=1$, all values of $\tilde{p}$ that support growth will satisfy the corresponding criteria. Both constants increase everywhere as δ and as K_* increase (Figure 12). Thus, larger specific-sinking-rate ratios δ and smaller half-saturation constants K favor the development of hypoxia.

The dependence of two constants on δ and K_*, while monotonic, is not linear (Figure 12). For both constants, the dependence on K_* is generally stronger for larger δ than for smaller δ (Figure 12). The smaller constant, P, which determines the production rate below which no hypoxic steady states occur, has a distinct change in dependence at $\delta=1$: for $\delta < 1$, P is independent of δ, while for $\delta > 1$, P decreases rapidly with δ. The larger constant, P', has a contrasting behavior, with a stronger dependence on δ for $\delta < 1$, and a smooth transition between the two regimes.

6. Discussion

The preceding analysis, while based on a highly idealized model, can be used to make rough estimates of hypoxic susceptibility for any upwelling system for which approximate values for the basic model parameters are available, as follows:

1. From values, or ranges of values, of the relevant half-saturation constant K, the source-water nutrient concentration N_s, and the specific-sinking-rate ratio $\delta=s'/s=(S'/H_{mid})/(S/H)$, the values of the constants P and $P\prime$ can be computed for a specific hypoxic threshold ΔO_{hyp} (Figure 12 or equations in Appendix A).

Hypoxia will generally be favored if these constants are close to one, and less favored if they are larger than one.

2. From values, or ranges of values, of the production, respiration, and upwelling rates, the dimensionless production rate $\tilde{p}=p/(r+\lambda)$ can be computed, and compared to the constants P and P' to provide a rough classification of the system as (1) likely, (2) able, or (3) unable to support hypoxia, where these cases correspond respectively to (1) $\tilde{p} > P\prime$, (2) $P < \tilde{p} < P'$, and (3) $\tilde{p} < P$. The sinking rate can be compared to the optimal rate (5.4); if it is much less than the optimal rate, then the classification will be conservative, and the susceptibility to hypoxia will be less than indicated.
3. From values, or ranges of values, of the production, respiration, sinking, and upwelling rates, as well as the sinking-rate ratio and the initial surface particle concentration, the maximal accumulation rate $\alpha=p-r-s-\lambda$ and the associated timescale t_{hyp} (4.4) for the onset of hypoxia can be computed. The timescale t_{hyp} can then be compared to the length of the relevant upwelling season, to estimate the likelihood that systems are potentially – based on comparisons of dimensionless production rate $\tilde{p}$ with the constants P and P'– able to support steady-state hypoxia will indeed be able to reach hypoxia seasonally.

The model, as formulated here, predicts rapid and extensive oxygen depletion across vast swaths of parameter space, encompassing many combinations typical of upwelling systems. When it does not predict hypoxia, it often exhibits unrealistic particle distributions, with far more accumulation in the surface than is ever observed and little accumulation at depth. These results therefore strongly suggest that most observed real-world systems have strong tendencies toward hypoxia, and the question then evolves from what controls the timing and extent of hypoxia to why hypoxia is not an even more prevalent feature of these systems. For the above analysis and considerations, the upwelling rate has been fixed in time. In many upwelling systems, however, the rate and intensity of upwelling varies strongly in time [*Carr*, 1998; *Perlin et al.*, 2005; *Bane et al.* 2007]. *Hales et al.* [2006] suggested that this modulation of the upwelling forcing presented an export pathway for the missing particle production over the Oregon shelf that should or would have led to far greater oxygen depletion than observed.

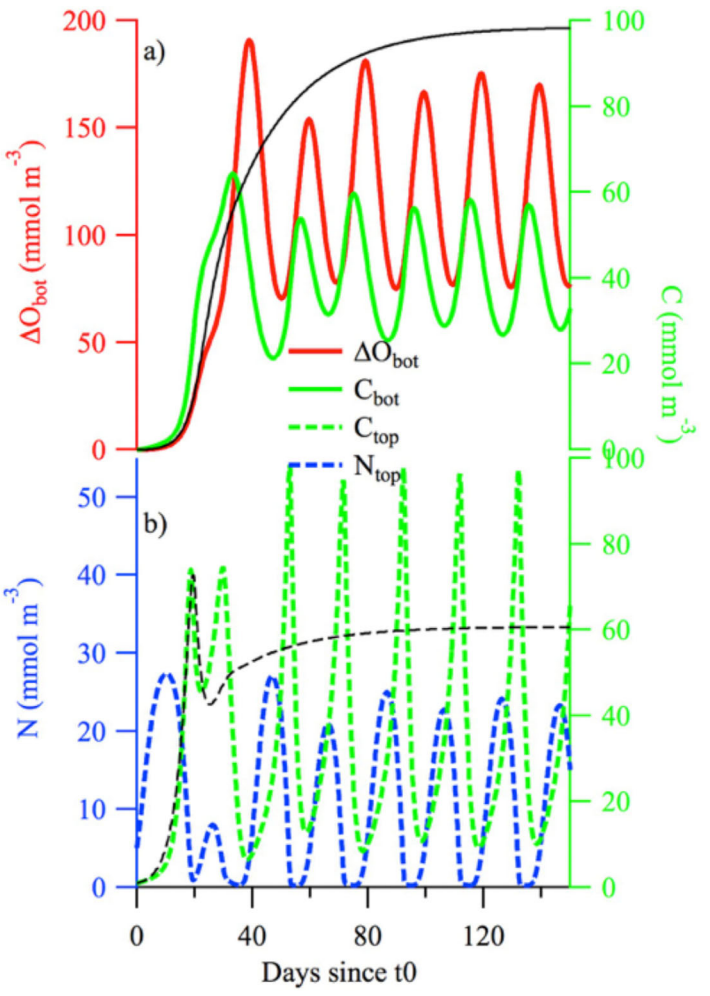

Figure 13. Solutions for FP as in Figure 2 but for oscillatory forcing as in (6.1). (a) Time-dependent solutions for ΔO_{bot} and C_{bot} (red and green solid lines, respectively). (b) Time-dependent solutions for C_{top} and N_{top} (green and blue dashed lines). Thin black lines show the time-dependent solutions for ΔO_{bot} (Figure 13a, solid line) and C_{top} (13b, dashed line) in the constant-forcing case (from Figures 2a and 2b).

Extensions of the present analysis, in which an oscillatory component is added to the upwelling rate, so that the system fluctuates between strong and weak or vanishing upwelling, indicate that time-

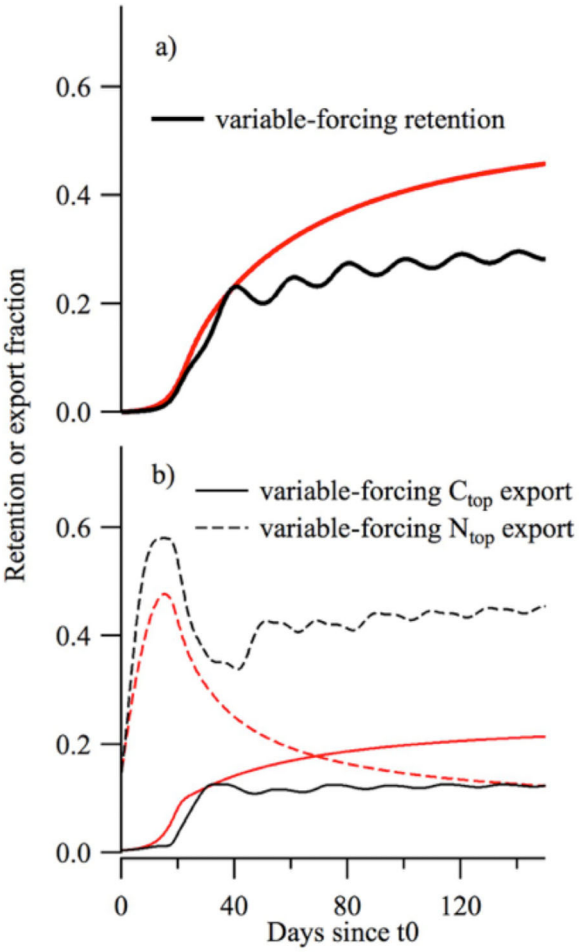

Figure 14. (a) Retention $c(t)$ from equations (3.2) and (b) export fractions for the variable forcing scenario with the FP parameter set. Red lines are the same as in Figure 4 for the FP case and are shown for comparison.

dependent forcing can significantly reduce the potential for oxygen depletion, relative to constant forcing cases with equivalent cumulative or time-mean forcing. For example, if the forcing in the FP case is modified to

$$\lambda'(t) = \lambda(1+\sin \varpi t), \tag{6.1}$$

so that the upwelling rate oscillates between 2λ and zero, but the mean forcing over an upwelling period is still λ, then the mean oxygen depletion is reduced by over 50 mmol m^{-3} relative to the steady-state value with constant forcing at rate λ (Figure 13). This reduction is accomplished via lowered retention efficiency (equation (3.2); Figure 14a), resulting from increased offshore transport of surface nutrients and/or particles, which reduces sinking export over the shelf and so also bottom oxygen depletion. This offshore transport occurs when there is a correlation of strong forcing with either high surface nutrient or particle levels. Figure 14b clearly shows, however, that the greatest loss of potential respiration is in the offshore transport of N_{top} during the maximal upwelling, which is much greater than for the constant-forcing case while offshore export of C_{top} is much less. The mechanism therefore is that the productivity cannot keep up with the fastest upwelling rates, and N_{top} is lost from the system before C_{top} is produced. There have been direct observations of this scenario. *Evans et al*. [2015] reported time-series data of surface signatures of productivity in response to a particularly intense upwelling event, and showed that the productivity response could not keep pace with the most intense upwelling. A more detailed study of this effect and the associated processes in this simple model is in progress and will be reported on separately.

Some conclusions about what these results may mean for the future as well as for present-day spatial variability in hypoxia can be drawn from the analysis presented here. The typical period of oscillation of winds in the northern California Current System (CCS) is 8 days [*Austin and Barth*, 2002], and has been suggested both to be getting longer and more intense [*Iles et al*., 2012] or, alternatively, to have no trend [*Bylhouwer et al*., 2013]. The productivity response to increased upwelling seen here is consistent with the suggestions of *Bakun et al*. [2015] and the observations of *Evans et al*. [2015], in that there is an ideal window or an optimal environmental range for productivity that results from a balance between the timescales of upwelled and offshore transport of nutrient and those of the autotrophic response. Our results build on that and suggest a negative feedback between increased upwelling and hypoxia, for other parameters constant: faster upwelling leads to less retention of respiration potential, and greater export of this potential to the open ocean where it can be more broadly laterally and vertically dispersed rather than being focused on shelf bottom waters.

For representative parameters and steady forcing, the predicted timescale for reaching mild hypoxia ($\Delta O_{bot} = 40$ mmol m^{-3}) is about 20 days (section 4.2; Figure 6), based on current oxygen levels in the source waters for the CCS. Those waters have been declining in oxygen at a rate of approximately 1 mmol m^{-3} yr^{-1} [*Bograd et al*., 2015; *Crawford and Peña*, 2013], and if that trend continues, the mild hypoxia

threshold defined here will instead approach the severe threshold in about 40 years, and specific O_{bot} criteria will be reached with even more rapidity. Along with this drop in O_s is a likely stoichiometric increase in N_s, which further amplifies this trend. Even if neither the mean wind forcing nor its modulation change significantly, more frequent severe hypoxic events can be anticipated in the future.

In addition, insights into mechanisms responsible for generating the spatial variability along the coast in the CCS can be explained, in part, by the analysis presented here. The wider shelves and weaker upwelling winds present in the northern part of the California Current System, for example, would reduce the upwelling forcing, allowing greater productivity response and retention of respiration in near-bottom waters over the shelf. The northern CCS experiences an increased occurrence of hypoxia relative to the south [*Peterson et al.*, 2013], which is consistent with the shorter oxygen drawdown times found there (Figure 6). In contrast, the winds are stronger and the shelves narrower farther south in the CCS, which is potentially what makes that region less susceptible to the respiratory potential and influenced more by the flushing of low-oxygen water from offshore.

7. Summary

A maximally simple, coupled physical-biogeochemical box model has been used to examine oxygen depletion near the shelf bottom in ocean-margin upwelling systems. It was found possible to achieve a relatively complete characterization of the bottom oxygen depletion response in this model. The major biogeochemical control on the overall potential susceptibility of the system was found to be the sinking rate s: for sufficiently small sinking rates, the system can never reach hypoxia even for arbitrarily long upwelling seasons, while the critical sinking rate allowing the system to approach hypoxia is nearly independent of the production rate p and maximal accumulation rate $\alpha = p - r - s - \lambda$. For sinking rates large enough that hypoxia could in principle be reached, the maximal accumulation rate was found to be the major control on the timescale of approach to hypoxia: for sufficiently large maximal accumulation rates, hypoxia can be reached in typical upwelling seasons, while for very small maximal accumulation rates, the time to hypoxia can exceed the length of typical upwelling seasons, and hypoxia – although possible in principle – cannot be reached.

The primary influence of the particle production rate on hypoxia in this model is indirect: larger production rates allow growth at larger sinking rates, and larger sinking rates increase oxygen depletion. Sinking velocities are poorly constrained by observations; however, if the sinking rate is presumed to be near the optimal rate for producing hypoxia, then the constraints on sinking rate translate into constraints on the production rate. Observations in upwelling systems of primary production are more prevalent than those of sinking rates and can even be garnered from satellite products. If rough estimates of the relevant rates and parameters are available for a given upwelling system, these can be used with the model results to obtain a basic characterization of the system's potential susceptibility to hypoxia that requires minimal computation (section 4).

In general, oxygen depletion in this model decreases with stronger upwelling forcing (Figures 5 and 7). To support hypoxia, the sinking rate must generally be comparable to the sum of the respiration and upwelling rates (Figure 8), with the precise relation depending on the sinking-rate ratio δ and other factors. Thus, for large upwelling rates, which can arise either from strong wind forcing or narrow shelf width, sinking must be rapid to support hypoxia, even for arbitrarily long upwelling seasons. Additionally, if hypoxia can occur and the system is forced sufficiently to overcome nutrient limitation, then the timescale for approach to hypoxia lengthens with stronger forcing, since particle production is shunted off-shelf and surface particle accumulation decreases, in turn reducing subsurface respiration and oxygen depletion. Together, these results suggest that if upwelling winds intensify with climate change [*Sydeman et al.*, 2014; *Bakun et al.*, 2015], the increased forcing could offer a mitigating effect on future coastal depletion events [e.g., *Evans et al.*, 2015], even as the oxygen levels in upwelled source waters decline [*Doney et al.*, 2012; *Bakun et al.*, 2015].

The analytical characterization of the physical-biogeochemical upwelling system presented here is possible only because of the many simplifications and idealizations in the model formulation. Many other influences on oxygen depletion, including effects of three-dimensional circulation and downwelling, and all the many complications of the biological and chemical transformations that are implicit in the model conversions between nutrients and particles, cannot be addressed within the framework of the present model, and require more sophisticated approaches with substantially more complex models. Achieving a similar level of general understanding of these more complex models remains an outstanding scientific challenge. The present work is intended as a preliminary step toward that broader understanding.

Appendix A

A1. Middle-Box Particle Concentration

The equation for the middle-box particle concentration $C_{mid}$is most conveniently posed in terms of the scaled concentration $C'_{mid}=(S'/S)C_{mid}$:

$$\frac{dC\prime_{mid}}{dt}=-rC'_{mid}-\delta sC'_{mid}+\delta sC_{top}. \tag{A1}$$

In this form, the sinking flux into the bottom box in (2.4) is $E_{bot}=(S'/H)C_{mid}=\ sC'_{mid}$, and the sinking rates and box thicknesses enter the model equations only through the single parameter δ. Multiplication of (A1a) by the integrating factor exp[-($r+\delta s$)t] and integration, using $C'_{mid0}=0$, then gives (2.6) directly. The equation (A1a) can be convenient to retain in place of (2.6) for numerical solution. For an impulsive sinking flux from the top box $E_{top}(t)=sC_{top}=E_0\delta_D(t)$ at $t=0$, where here δ_D is the Dirac-δ impulse, the incoming sinking flux to the bottom is $E_{bot}(t>0)=\ \delta sE_0\exp[-(r+\delta s)t]$ and its total time-integral is $\int_0^\infty E_{bot}(t)dt=\ E_0/[1+r/(\delta s)]$, illustrating that attenuation of the sinking flux from the top to the bottom boxes is largest for large r and small δs.

A2. Total Nutrient Equivalent and N_{bot}-O_{bot} Coupling

Summing the particle and nutrient equations, with the former divided by γ, gives an equation for the evolution of total nutrient equivalent, $\mathcal{N}$, where $\mathcal{N}=\ N_{bot}+N_{top}+\ \gamma^{-1}\left(C_{bot}+\delta_H^{-1}C_{mid}+C_{top}\right)$:

$$\frac{d\mathcal{N}}{dt}=\ \lambda N_s-\lambda\left(N_{top}+\gamma^{-1}C_{top}\right)-r\delta_H^{-1}C_{mid}. \tag{A2}$$

Thus, in steady state, onshore nutrient transport into the bottom box is balanced by losses from offshore transport out of the top box and from middle-box respiration.

In this model, bottom nutrients and oxygen are tightly coupled: the respiration (C_{bot}) sink and source terms cancel from (2.1) and v times (2.3) when these equations are summed, leaving only the advective relaxation of the sum $O_{bot}\ +\ v\ N_{bot}$ toward its offshore value $O_s\ +\ v\ N_s$. Consequently, if, as here, bottom-box oxygen and nutrient concentrations are initially equal to their offshore values, or steady states are considered, either (2.1) or (2.3) could in principle be replaced by the relation

$$\Delta O_{bot}=\ v\ (N_{bot}-N_s). \tag{A3}$$

In general, of course, (A3) does not hold, and to avoid possible confusion, (2.1) and (2.3) are therefore both retained throughout.

A3. Steady States

The explicit (nontrivial) steady state solutions of (2.1)–(2.5) and (A1), with $E_{bot}=\ sC'_{mid}$ in (2.2), are:

$$\overline{\Delta O_{bot}}=\frac{rv}{\lambda\gamma}\overline{C_{bot}}, \tag{A4}$$

$$\overline{C_{bot}}=\frac{s}{r}\overline{C_{mid}}, \tag{A5}$$

$$\overline{C_{mid}}=\frac{\delta s}{r+\delta s}\overline{C_{top}}, \tag{A6}$$

$$\overline{C_{top}}=\frac{(r+\delta s)\lambda}{rs+(r+\delta s)\lambda}\gamma\left(N_s-\overline{N_{top}}\right), \tag{A7}$$

$$\overline{N_{top}}=\frac{r+s+\lambda}{p-r-s-\lambda}K=\frac{p_*K_*}{\alpha}N_s, \tag{A8}$$

$$\overline{N_{bot}}=N_s+\frac{r}{\lambda\gamma}\overline{C_{bot}}=N_s+\frac{1}{v}\overline{\Delta O_{bot}}. \tag{A9}$$

From (A7), it follows that $\overline{N_{top}}<N_s$ for all states with $\overline{C_{top}}>0$, and from (A4) to (A8) that $\overline{N_{top}}=\overline{N_{bot}}=N_s$ and $\overline{C_{top}}=\overline{C_{bot}}=\overline{\Delta O_{bot}}=0$ when $p=p_*$, where $p_*=(r+s+\lambda)/N_*$, because then also $\alpha=\alpha_*=p_*-r-s-\lambda=p_*K_*$.

A4. Optimal Sinking and Constants P, P'

The sinking rate $s=s_{opt}$ at which $\overline{\Delta O_{bot}}$ is maximum (i.e., where $d\left(\overline{\Delta O_{bot}}\right)/ds=0$, with all other parameters fixed) can be obtained as a solution of the cubic equation

$$s^3+as^2+bs+c=0, \tag{A10}$$

where

$$a=2(\lambda R-s_{\max}),\ \ b=s_*s_{\max}-\lambda R(s_*+3s_{\max})\ \ c=2\lambda Rs_*s_{\max}, \tag{A11}$$

with $R=r/(r+\delta\lambda)=1/(1+\delta\Lambda)$. For sufficiently small λpRK_* (typically satisfied because $K \ll N_s$), the cubic (A10) approximately factors and the approximation (5.4) for the optimal sinking rate may be obtained as a solution of the quadratic part.

The steady states with $\overline{\Delta O_{bot}}=\Delta O_{hyp}$ at the optimal sinking rate $s=s_{opt}$ satisfy

$$\Delta O_{hyp}=\frac{\delta Rs_{opt}^3}{rs_{\max}\left(s_{opt}+\lambda R\right)}v(K+N_s), \tag{A12}$$

where the sinking rate s_{opt} is optimal over s for fixed r and λ. For fixed p and $s_{\max}$, an optimal r can be found by substituting $\lambda=p-s_{\max}-r$ in (A12) and maximizing over r. This maximum of ΔO_{hyp}, regarded as a function of r, is at $r=0$ for $\delta<1$, and at $r=p-s_{\max}$ for $\delta>1$. The resulting sufficient condition (section 5.4) for the existence of hypoxic states (for some r, with fixed $p-s_{\max}$ and $s=s_{opt}$) is

$$p-s_{\max}=r+\lambda \le p/P, \tag{A13}$$

where

$$P=\frac{\xi^2}{\xi^2-1}, \tag{A14}$$

and

$$\xi=\frac{(1+N_*A_\delta)^{1/2}-K_*^{1/2}A_\delta}{1-K_*A_\delta}\ , A_\delta=\max\{1,\delta\}A,\ A=\frac{v(K+N_s)}{\Delta O_{hyp}}. \tag{A15}$$

Alternatively, minimization of (A12), again with fixed $p-s_{\max}$ (i.e., $\lambda=p-s_{\max}-r$) and $s=s_{opt}$, gives a quartic in the variable $q=\sqrt{p/s_{\max}}$, one solution of which gives the sufficient condition for hypoxic steady states at any r or, equivalently, any Λ (section 5.4),

$$p-s_{\max}=r+\lambda \le p/P'\ . \tag{A16}$$

The corresponding quartic equation for q is

$$q^4+a_qq^3+b_qq^2+c_qq+d_q=0, \tag{A17}$$

where

$$a_q=2K_*^{1/2}[2K_*\delta A-(1+\delta)], \tag{A18a}$$

$$b_q=2\delta+K_*(1-\delta)^2-12K_*\delta A, \tag{A18b}$$

$$c_q=2K_*^{1/2}\delta(3-\delta+6A), \tag{A18c}$$

$$d_q=\delta[\delta-4(1+A)], \tag{A18d}$$

and A is defined in (A15).

Acknowledgments

This research was supported by the National Science Foundation, grant OCE-1130114. CSH is grateful for helpful conversations with M. Hoecker-Martinez and C. Miller. No new observational data are reported in this manuscript and all of the results and figures were obtained using standard numerical or analytical methods to solve the model equations; for further details, contact the corresponding author at the email address given on the title page (rsamelson@coas.oregonstate.edu).

References

Adams, K. A. (2014), Influence of upwelling-season coastal currents on near-bottom dissolved oxygen concentrations over a submarine bank, 144 pp., PhD thesis, Oceanography, Oreg. State Univ., Corvallis, Oreg.

Adams, K. A., J. A. Barth, and F. Chan (2013), Temporal variability of near-bottom dissolved oxygen during upwelling off central Oregon, *J. Geophys. Res. Oceans*, *118*, 4839–4854, doi:10.1002/jgrc.20361.

Austin, J. A., and J. A. Barth (2002), Variation in the position of the upwelling front on the Oregon shelf, *J. Geophys. Res.*, *107*(C11), 3180, doi:10.1029/2001JC000858.

Bailey, G. W. (1991), Organic carbon flux and development of oxygen deficiency on the modern Benguela continential shelf south of 22°S: Spatial and temporal variability, *Geol. Soc. Spec. Publ.*, *58*, 171–183, doi:10.1144/GSL.SP.1991.058.01.12

Bailey, G. W., C. J. De B. Beyers, and S. R. Lipschitz (1985), Seasonal variation of oxygen deficiency in waters off southern South West Africa in 1975 and 1976 and its relation to the catchability and distribution of the Cape rock lobster Jasus lalandii, *S. Afr. J. Mar. Sci.*, *3*(1), 197–214, doi:10.2989/025776185784461126.

Bakun, A., B. A. Black, S. J. Bograd, M. García-Reyes, A. J. Miller, R. R. Rykaczewski, and W. J. Sydeman (2015), Anticipated effects of climate change on coastal upwelling ecosystems, *Curr. Clim. Change Rep.*, *1*(2), 85–93, doi:10.1007/s40641-015-0008-4.

Bakun, A. B. (1990), Global climate change and intensification of coastal ocean upwelling, *Science*, *247*, 198–201.

Bane, J. M., Y. H. Spitz, R. M. Letelier, and W. T. Peterson (2007), Jet stream intraseasonal oscillations drive dominant ecosystem variations in Oregon's summertime coastal upwelling system, *Proc. Natl. Acad. Sci. U. S. A.*, *104*(33), 13,262–13,267, doi:10.1073/pnas.0700926104.

Barber, R. T., and F. P. Chavez (1991), Regulation of primary productivity rate in the equatorial Pacific, *Limnol. Oceanogr.*, *36*(8), 1803–1815, doi:10.4319/lo.1991.36.8.1803.

Bianucci, L., K. L. Denman, and D. Ianson (2011), Low oxygen and high inorganic carbon on the Vancouver Island Shelf, *J. Geophys. Res.*, *116*, C07011, doi:10.1029/2010JC006720.

Bograd, S. J., C. G. Castro, E. Di Lorenzo, D. M. Palacios, H. Bailey, W. Gilly, and F. P. Chavez (2008), Oxygen declines and the shoaling of the hypoxic boundary in the California Current, *Geophys. Res. Lett.*, *35*, L12607, doi:10.1029/2008GL034185.

Bograd, S. J., M. P. Buil, E. D. Lorenzo, C. G. Castro, I. D. Schroeder, R. Goericke, C. R. Anderson, C. Benitez-Nelson, and F. A. Whitney (2015), Changes in source waters to the Southern California Bight, *Deep Sea Res., Part II*, *112*, 42–52, doi:10.1016/j.dsr2.2014.04.009.

Bylhouwer, B., D. Ianson, and K. Kohfeld (2013), Changes in the onset and intensity of wind-driven upwelling and downwelling along the North American Pacific coast, *J. Geophys. Res. Oceans*, *118*, 2565–2580, doi:10.1002/jgrc.20194.

Carr, M.-E. (1998), A numerical study of the effect of periodic nutrient supply on pathways of carbon in a coastal upwelling regime, *J. Plankton Res.*, *20*(3), 491–516, doi:10.1093/plankt/20.3.491.

Carr, M.-E., and E. J. Kearns (2003), Production regimes in four Eastern Boundary Current systems, *Deep Sea Res., Part II*, *50*(22–26), 3199–3221, doi:10.1016/j.dsr2.2003.07.015.

Chai, F., R. C. Dugdale, T. H. Peng, F. P. Wilkerson, and R. T. Barber (2002), One-dimensional ecosystem model of the equatorial Pacific upwelling system. Part I: Model development and silicon and nitrogen cycle, *Deep Sea Res., Part II*, *49*(13–14), 2713–2745, doi:10.1016/S0967-0645(02)00055-3.

Chan, F., J. A. Barth, J. Lubchenco, A. Kirincich, H. Weeks, W. T. Peterson, and B. A. Menge (2008), Emergence of anoxia in the California Current Large Marine Ecosystem, *Science*, *319*(5865), 920, doi:10.1126/science.1149016.

Chavez, F. P., and M. Messié (2009), A comparison of Eastern Boundary Upwelling Ecosystems, *Prog. Oceanogr.*, *83*(1–4), 80–96, doi:10.1016/j.pocean.2009.07.032.

Chavez, F. P., and J. Toggweiler (1995), Physical estimates of global new production: The upwelling contribution, in *Upwelling in the Ocean: Modern Processes and Ancient Records*, edited by C. P. Summerhayes, et al., pp. 313–320, Wiley, N. Y.

Connolly, T. P., B. M. Hickey, S. L. Geier, and W. P. Cochlan (2010), Processes influencing seasonal hypoxia in the northern California Current System, *J. Geophys. Res.*, *115*, C03021, doi:10.1029/2009JC005283.

Crawford, W. R., and M. A. Peña (2013), Declining oxygen on the British Columbia Continental Shelf, *Atmos. Ocean*, *51*(1), 88–103, doi:10.1080/07055900.2012.753028.

Deutsch, C., H. Brix, T. Ito, H. Frenzel, and L. Thompson (2011), Climate-forced variability of ocean hypoxia, *Science*, *333*(6040), 336–339, doi:10.1126/science.1202422.

Doney, S. C., et al. (2012), Climate change impacts on marine ecosystems, *Annu. Rev. Mar. Sci.*, *4*(1), 11–37, doi:10.1146/annurev-marine-041911-111611.

Dugdale, R. C., and F. P. Wilkerson (1998), Silicate regulation of new production in the equatorial Pacific upwelling, *Nature*, *391*(6664), 270–273, doi:10.1038/34630.

Evans, W., B. Hales, P. G. Strutton, R. K. Shearman, and J. A. Barth (2015), Failure to bloom: Intense upwelling results in negligible phytoplankton response and prolonged CO_2 outgassing over the Oregon shelf, *J. Geophys. Res. Oceans*, *120*, 1446–1461, doi:10.1002/2014JC010580.

Gill, A. E. (1982), *Atmosphere-Ocean Dynamics*, 662 pp., Academic, N. Y.

Grantham, B. A., F. Chan, K. J. Nielsen, D. S. Fox, J. A. Barth, A. Huyer, J. Lubchenco, and B. A. Menge (2004), Upwelling-driven nearshore hypoxia signals ecosystem and oceanographic changes in the northeast Pacific, *Nature*, *429*(6993), 749–754, doi:10.1038/nature02605.

Hales, B., J. N. Moum, P. Covert, and A. Perlin (2005), Irreversible nitrate fluxes due to turbulent mixing in a coastal upwelling system, *J. Geophys. Res.*, *110*, C10S11, doi:10.1029/2004JC002685.

Hales, B., L. Karp-Boss, A. Perlin, and P. A. Wheeler (2006), Oxygen production and carbon sequestration in an upwelling coastal margin, *Global Biogeochem. Cycles*, *20*, GB3001, doi:10.1029/2005GB002517.

Herrera, J. L., G. Rosón, R.A. Varela, and S. Piedracoba (2008), Variability of the western Galician upwelling system (NW Spain) during an intensively sampled annual cycle. An EOF analysis approach, *J. Mar. Syst.*, *72*, 200–217, doi:10.1016/j.jmarsys.2007.07.007.

Holser, R. R., M. A. Goni, and B. Hales (2011), Design and application of a semi-automated filtration system to study the distribution of particulate organic carbon in the water column of a coastal upwelling system, *Mar. Chem.*, *123*(1–4), 67–77, doi:10.1016/j.marchem.2010.10.001.

Iles, A. C., T. C. Gouhier, B. A. Menge, J. S. Stewart, A. J. Haupt, and M. C. Lynch (2012), Climate-driven trends and ecological implications of event-scale upwelling in the California Current System, *Global Change Biol.*, *18*(2), 783–796, doi:10.1111/j.1365-2486.2011.02567.x.

Iversen, M. H., and H. Ploug (2010), Ballast minerals and the sinking carbon flux in the ocean: Carbon-specific respiration rates and sinking velocity of marine snow aggregates, *Biogeosciences*, *7*(9), 2613–2624, doi:10.5194/bg-7-2613-2010.

Iversen, M. H., and H. Ploug (2013), Temperature effects on carbon-specific respiration rate and sinking velocity of diatom aggregates - potential implications for deep ocean export processes, *Biogeosciences*, *10*(6), 4073–4085, doi:10.5194/bg-10-4073-2013.

Jamart, B. M., D. F. Winter, K. Banse, G. C. Anderson, and R. K. Lam (1977), A theoretical study of phytoplankton growth and nutrient distribution in the Pacific Ocean off the northwestern U.S. coast, *Deep Sea Res.*, *24*(8), 753–773, doi:10.1016/0146-6291(77)90498-2.

Karp-Boss, L., P. A. Wheeler, B. Hales, and P. Covert (2004), Distributions and variability of particulate organic matter in a coastal upwelling system, *J. Geophys. Res.*, *109*, C09010, doi:10.1029/2003JC002184.

Keller, A. A., L. Ciannelli, W. W. Wakefield, V. Simon, J. A. Barth, and S. D. Pierce (2015), Occurrence of demersal fishes in relation to near-bottom oxygen levels within the California Current large marine ecosystem, *Fish. Oceanogr.*, *24*(2), 162–176, doi:10.1111/fog.12100.

Lindley, S. T., R. R. Bidigare, and R. T. Barber (1995), Phytoplankton photosynthesis parameters along 140°W in the equatorial Pacific, *Deep Sea Res., Part II*, *42*(2–3), 441–463, doi:10.1016/0967-0645(95)00029-P.

McClatchie, S., R. Goericke, R. Cosgrove, G. Auad, and R. Vetter (2010), Oxygen in the Southern California Bight: Multidecadal trends and implications for demersal fisheries, *Geophys. Res. Lett.*, *37*, L19602, doi:10.1029/2010GL044497.

McDonnell, A. M. P., and K. O. Buesseler (2010), Variability in the average sinking velocity of marine particles, *Limnol. Oceanogr. Methods*, *55*(5), 2085–2096, doi:10.4319/lo.2010.55.5.2085.

McDonnell, A. M. P., and K. O. Buesseler (2012), A new method for the estimation of sinking particle fluxes from measurements of the particle size distribution, average sinking velocity, and carbon content, *Limnol. Oceanogr. Methods*, *10*(5), 329–346, doi:10.4319/lom.2012.10.329.

Nam, S., H.-J. Kim, and U. Send (2011), Amplification of hypoxic and acidic events by La Niña conditions on the continental shelf off California, *Geophys. Res. Lett.*, *38*, L22602, doi:10.1029/2011GL049549.

Peña, M. A. S. Katsev, T. Oguz, and D. Gilbert (2010), Modeling dissolved oxygen dynamics and hypoxia, *Biogeosciences*, *7*, 933–957.

Perlin, A., J. N. Moum, and J. M. Klymak (2005), Response of the bottom boundary layer over a sloping shelf to variations in alongshore wind, *J. Geophys. Res.*, *110*, C10S09, doi:10.1029/2004JC002500.

Peterson, J. O., C. A. Morgan, W. T. Peterson, and E. D. Lorenzo (2013), Seasonal and interannual variation in the extent of hypoxia in the northern California Current from 1998–2012, *Limnol. Oceanogr. Methods*, *58*(6), 2279–2292, doi:10.4319/lo.2013.58.6.2279.

Ryther, J. H. (1969), Photosynthesis and fish production in the sea, *Science*, *166*(3901), 72–76, doi:10.1126/science.166.3901.72.

Schwing, F., M. O'Farrell, J. Steger, and K. Baltz (1996), Coastal upwelling indices, west coast of North America 1946-95, *Tech. Rep. NOAA-TM-NMFS-SWFSC-231*, 207 pp., Natl. Oceanic and Atmos. Admin., Silver Spring, Md.

Send, U., and S. Nam (2012), Relaxation from upwelling: The effect on dissolved oxygen on the continental shelf, *J. Geophys. Res.*, *117*, C04024, doi:10.1029/2011JC007517.

Siedlecki, S. A., N. S. Banas, K. A. Davis, S. Giddings, B. M. Hickey, P. MacCready, T. Connolly, and S. Geier (2015), Seasonal and interannual oxygen variability on the Washington and Oregon continental shelves, *J. Geophys. Res. Oceans*, *120*, 608–633, doi:10.1002/2014JC010254.

Sydeman, W. J., M. García-Reyes, D. S. Schoeman, R. R. Rykaczewski, S. A. Thompson, B. A. Black, and S. J. Bograd (2014), Climate change and wind intensification in coastal upwelling ecosystems, *Science*, *345*(6192), 77–80, doi:10.1126/science.1251635.

Wetz, M., B. Hales, and P. A. Wheeler (2008), Degradation of diatom-derived dissolved and particulate organic matter: Implications for coastal C and N biogeochemistry, *Estuarine Coastal Shelf Sci.*, *77*(3), 422–432, doi:10.1016/j.ecss.2007.10.002.